uc3m | Universidad Carlos III de Madrid

University Degree in Aerospace Engineering

Academic Year 2018-2019

Bachelor Thesis

"Design of an attitude control algorithm based on data from a single horizon sensor"

Alberto Jódar Moya

Javier Rodríguez Rodríguez

Leganés, June 2019

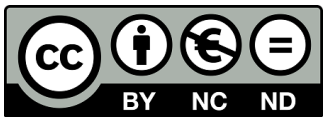

SUMMARY

Keywords: satellite, space, orbit, smallsat, CubeSat, gravity gradient, torque, angular velocity, Euler angles, algorithm, Mean Square Error

DEDICATION

First of all, I want to thank my professor *Javier Rodríguez*, for being an extraordinary guide for the project. Thank you for introducing this project to me, it has been a lot of fun.

To the guys, because my university experience would not have been the same.

To my family, thank you. Thank you for being always and always and always there. I'm sure I would not have been able to make it without your support. Thanks for believing in a different lifestyle. Thank you for believing in me.

CONTENTS

LIST OF FIGURES

LIST OF TABLES

1. INTRODUCTION

The idea of outer space has always been an enigma for the humans before the second half of the XIX century. After the devastating effects of the airplanes during World War I and II, the population was slowly getting used to fly; kids were raised staring at the blue skies, probably looking for any of those *huge metallic flying machines*, the number of which was increasing rapidly. It was not until October 4th, 1957 that the Russians launched the first artificial Earth satellite into a low orbit and for just three weeks. This was one of the milestones achieved by the Soviet Union at the beginning of the Cold War (1947-1991); however, only 4 years later, Yuri Gagarin surfed the space inside the famous Vostok-1 for 89 minutes at an approximate speed of 27400 kilometers per hour. Impressive. The Space Race had begun and USA was not going to step aside. On July 20th, 1969, after years of hard work, dedication and more importantly, counting on disproportionate budgets, the Apollo program succeeded and Neil Armstrong became the first human to step on the moon. That historical fact captivated a very large part of the world's population (little over 600 million people watched it), who started to rethink the *old* idea about the human inability to navigate through space. The Moon landing was definitely the spark that initiated the blaze that Space Industry is nowadays.

The space industry has evolved exponentially since then, well known international manufacturers like Airbus, Boeing or Lockheed Martin are playing an important role in the *battle* to build (and launch) the most extensive, efficient and profitable satellite network. In the last years, private companies like Blue Origin or SpaceX have revolutionized the industry by working on new ways to sell the space business, like for example, private spaceflights. Earlier this year, in March, SpaceX launched the Crew Dragon Test Flight to Space Station for NASA [1] which entailed a huge leap towards human spaceflight.

Latest reports show that there are approximately 4987 satellites orbiting the Earth at this moment [2], and surprisingly, only 1957 of them are active, little less than 40% of them. Interesting. More than half of them belong to USA and China (830 and 280 respectively) and 846 were launched for commercial use. Other practices include government, military and civil which together with the commercial use sum up to 89% of the total use.

One of the most important events that is contributing to the expansion of the satellite network is the proliferation of smallsats. Fast advances in technology, leading to a reliability and performance increase along with cheaper manufacturing techniques and processes have facilitated the launch of over 1300 satellites in the last 6 years, being the famous CubeSat the dominant player with 961 launches between 2012 and 2018 [3]. With an average mass of 55kg, these little satellites can be launched through LVs (Launching Vehicles) or directly from the International Space Station. Although the mean price for a LV has not decreased significantly, compared with smallsats, it is expected to do it in the following years so further and broader constellations of smallsats are forecast for the

future.

1.1. State of the art

As it was mentioned before, the advances in the vast majority of the components of the smallsats have promoted its use to the extent that almost any university, research center or individual, with *little* investment, is able to launch one. Minimum investment have been about $150,000 [4] ($50,000 for manufacturing and $100,000 for launching) which makes it quite affordable for small users of both commercial and scientific areas. Development of lighter materials for the satellite's structure, more efficient solar panels and batteries for the electrical power system and improved electronics for attitude determination, control and general onboard computing are just few examples that show the significant moment this sector is living.

Despite CubeSats were initially thought to be used in a low orbit environment, between those 961 launched there are two examples of a more ambitious application [5]: the interplanetary mission. The success of these two CubeSats, which accompanied the InSight on its mission to Mars, was a clear proof of the place that CubeSats deserve within the future of space exploration.

However, among all the CubeSat systems, the one concerning this work is the attitude determination and control system (ADCS), and more precisely, the first one. Different sensors are used for attitude determination, such as Sun sensors, star trackers, magnetometers and horizon sensors, but it is really the latter the one that is able to provide nearly uninterrupted fine attitude knowledge [6]. The previous fact along with an inexpensive manufacturing and improvements in the infrared detection technology had considerably contributed to their implementation in the CubeSats, accomplishing a 1σ nadir estimation error of less than 0.2 degrees.

1.2. Socio-economic impact

The development of cheaper and more efficient smallsats is causing the satellite manufacturing and launch industry to grow year after year. The global market revenues where of $277M in 2018 [7], of which half of them were related to satellite services like mobile and broadband or TV and transponder leasing. However, the largest increase in revenues were found in the launch industry, with an increment of 34% in 2018.

Related to the communications and broadcasting industry, OneWeb Satellites, the joint venture between Airbus and OneWeb, has recently launched its first batch of 5G satellites that will provide fast internet access everywhere in the Earth [8]. The company's plan is to had deployed a total of 650-satellites by 2020, which directly competes with SpaceX's Starlink project of putting up 12000 satellites, being able to go live by summer 2020 once 800 of them have been launched.

Nonetheless, as it is known, not everything related with progress is positive. Space debris is a problem that could create serious consequences in the future. First scenario, caused by debris reentring the Earth's atmosphere, like the Tiangong-1 case, where even being an uncontrolled reentry, it was completely expected and monitored [9]. Second scenario and more important, the density of the objects orbiting the Earth. Companies providing satellite constellations should also be able to guarantee the proper elimination of the malfunctioning or inactive old satellites in order to avoid the disastrous Kessler effect [10].

1.3. Motivation

The exponential growth that the space, and in particular, the satellite industry is experiencing is highly interesting. It brings the opportunity to develop new skills related to a topic that means present and future. Personally, I think is quite a challenge to develop a code that its meant to simulate a *real* situation that is to be happening at an altitude of hundreds or thousands of kilometers. Besides, as an engineer about to finish his degree, I find it quite satisfying to end my career applying the tools acquired at university to write an algorithm capable of solving a certain problem and subsequently, interpreting those results to give them validity. Professionally, I believe that earning some experience about space-related topics will always bring good chances to aim for a good job offers.

1.4. Objectives

The aim of this work is to develop an optimization algorithm using MATLAB that is able to determine the attitude of a slender body satellite when this is close to Earth-pointing nominal conditions. The algorithm uses exclusively as inputs the simulated data extracted from the implementation of two single horizon sensors.

1.5. Outline

In chapter 1 an introduction to the topic of the work is included. State of the Art, socio-economic impact, motivation of the project, main objectives and project outline are also included

Chapter 2 includes the description of the model and the assumptions stated. Satellite's body and orbit are defined as well as a brief introduction to the horizon sensor operation.

Chapter 3 exposes all the mathematical considerations of the problem and the strategy to solve it. A complete description of the algorithm operation is also included.

Chapter 4 contains the analysis and interpretation of the results of the different simulations carried out. Besides, results showing the accuracy of the algorithm in several ranges of study are also included.

Chapter 5 includes the conclusions of the work, focusing on the initial assumptions and how they could differ from reality.

Chapter 6 includes a set of ideas for a future work that increase the boundaries of the problem in order to provide a more realistic approach of it.

2. MODEL DESCRIPTION

In this chapter, the general characteristics of the satellite's body and orbit will be described. Besides, the basic operation of the horizon sensor simulated in the work is explained.

2.1. Satellite's Model

The satellite's body selected for this work was chosen based on the CubeSat 3U standard model [11]. However it has been modified in order to obtain a true slender body vehicle. The following properties are listed:

- Dimensions: x=0.1m y=0.1m z=1.55m (x:length y:width z:height)
- Mass: 1.33 kg
- $I_x = I_y = 0.266\ kgm^2 \quad I_z = 0.0022\ kgm^2 \quad \frac{I_z}{I_x} \approx 120.9$

In figure 2.1 is shown the standard version of a CubeSat 3U in which the model is based. As it was said before the satellite's body is assumed to be slender so its height has been incremented substantially. Is not in the scope of this work to analyze the structural implications of such a slender body, but it is sure that they must be studied carefully.

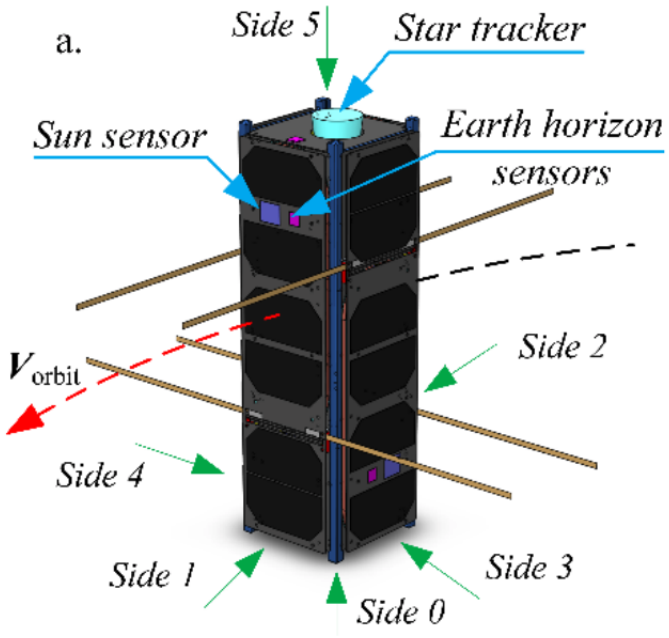

Fig. 2.1. Standard CubeSat 3U model

In addition, figure 2.1 shows the possible locations of the different attitude determination sensors, such as star trackers, Sun sensors and horizon sensors. Another example of a 3U CubeSat satellite model and its characterization can be found on [12]. However, this work is exclusively focused on the operation of the horizon sensor, in this way in section 3.6 the position and collocation of the cameras is completely explained.

2.2. Horizon Sensor

Earth horizon sensors picture the proximity of the Earth horizon (also called limb) to locate the non-thermal airglow emissions. They detect the interface between the Earth's edge and the space background [13]. Two main categories of horizon sensors can be found, *scanning* and *static*. Scanning type scans the Earth pursuing the horizon crossings and measuring the time span between horizon crossings. In static type however, the picture of the horizon is captured onto an infrared detector array so it allows the limb to be determined from the image. The range or field of view of a static horizon sensor is sometimes larger than the complete Earth's horizon.

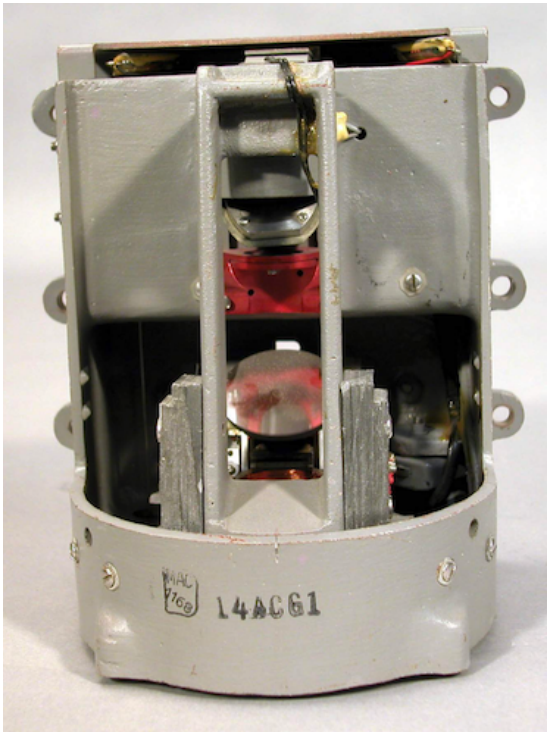

Fig. 2.2. Example of a static horizon sensor used in the *Gemini* space capsule. Taken from [14]

2.2.1. Information obtained from one horizon sensor

The document [15] is going to be used as reference to explain the mathematical aspects of the operation of the horizon sensor. First of all, the basic geometry of the problem is pictured in figure 2.3, where the sphere of attitude of the satellite is draw,

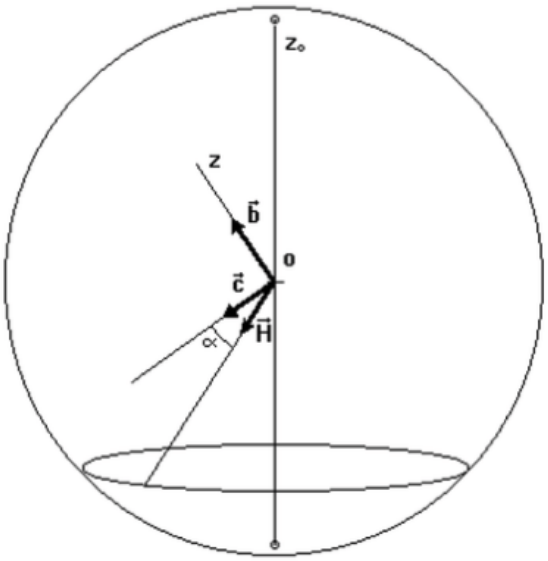

Fig. 2.3. Attitude sphere representation

where z_0 is the document's orbit fixed Z axis, z is the body fixed Z axis, $\vec{b}$ is the sweep vector, usually linked to z, $\vec{c}$ is the camera's line of vision and $\vec{H}$ is the horizon vector as seen by the camera. The latter is defined as the vector pointing to the intersection of the plane formed by vectors $\vec{b}$ and $\vec{c}$ with the projection of the Earth's horizon over the sphere of attitude, in section 3.6 is explain in more detail. The angle of interest is the one formed by the vectors $\vec{c}$ and $\vec{H}$, α.

The final step is obtaining the angle α from the infrared detector array image as follows

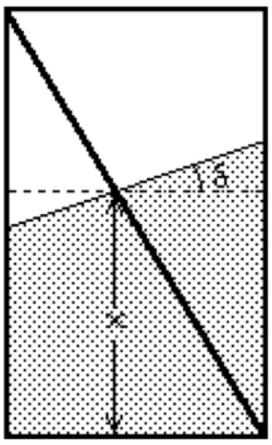

Fig. 2.4. example of image taken from a infrared detector array

from figure 2.4 two angles are defined, the inclination angle δ and α. The following equations are obtained taking into account the illuminated areas on left and right cells and

the total height h and width w of them.

$$L_{area} = wx - \frac{wx^2}{2h} - \frac{w^2}{h^2}\left(h^2 - 2hx + x^2\right)\frac{tan\delta}{2} \tag{2.1}$$

$$R_{area} = \frac{wx^2}{2h} + \frac{w^2}{h^2}x^2\frac{tan\delta}{2} \tag{2.2}$$

Solving for $tan\delta$ in both equations and equating them, the following quadratic equation is obtained

$$\left(R_{area} + L_{area} - \frac{wh}{2}\right)x^2 - 2hR_{area}x + R_{area}h^2 = 0 \tag{2.3}$$

Solving for x and using the hypothesis of a small δ to discriminate one of the two solutions [15], the angle x or α is obtained.

It is important to remark that the information retrieved from the operation of one sensor is insufficient to determine the satellite's attitude with exactness. The precision in the calculation of the angle δ is low. In consequence, for a complete, more accurate determination of the attitude, two sensors will be used.

2.3. Satellite's Orbit

In order to simplify the calculations, the selected orbit is perfectly circular. Main characteristics are written below

- Type: circular
- Altitude: 998 [km] Low Earth Orbit (LEO)
- Angular velocity: Ω=0.001 [rad/s]
- Period: 6283.19 [s] $\approx$ 1.75 [h]

In order to get a visual reference, the following plot shows the top view representation of the orbit in a random instant in time.

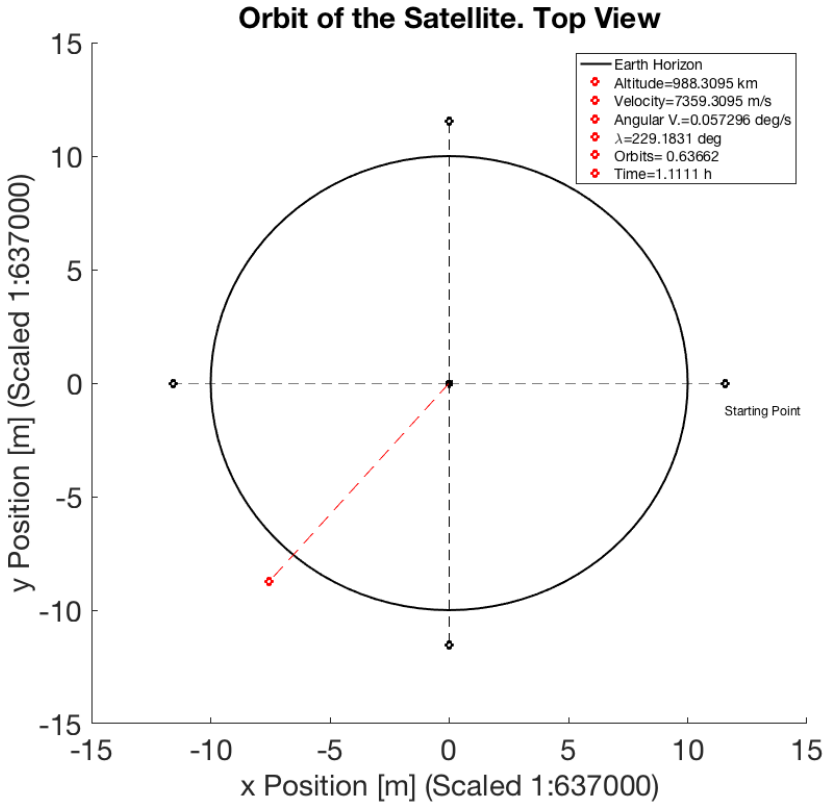

Fig. 2.5. scaled satellite's orbit and significant data

3. METHODOLOGY

The physical model proposed by this work is a slender body satellite orbiting around the Earth by the effect of the gravity gradient. In this chapter, the problem will be completely defined and both physical and mathematical aspects will be exposed following the same criteria as [16] and [15]. All the assumptions stated for the model and its expected limitations will described as well. Finally, a strategy to solve it will be proposed.

3.1. Coordinate systems

Firstly, the coordinate systems used for determining the rotation of the satellite will be defined following the same principles as [16].

3.1.1. Perifocal Coordinate System

This coordinate system is very close to be inertial, which will be the base for our description of the Euler equations later. The origin is placed at the Earth's center, the Y axis is perpendicular to the orbits plane, the Z axis is directed to the perigee and finally, X is defined following the right hand's rule with Y and Z. This system of coordinates is found below:

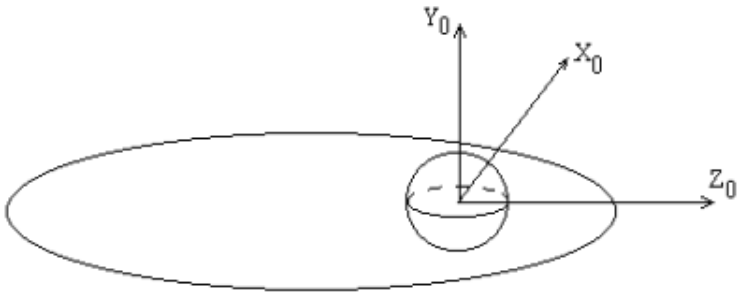

Fig. 3.1. Perifocal Coordinate System

The system is considered to be inertial although the orbit is not fixed, as it experiences a small precession. This effect will be neglected for the sake of simplicity and due to the fact that is a much slower movement compared to the ones studied in this work. The unitary vectors are $\vec{I_0}$, $\vec{J_0}$ and $\vec{K_0}$.

3.1.2. Orbit Fixed Coordinate System

The orbit is perfectly circular with constant angular velocity so the attitude of the satellite is defined with respect to this system. The Z axis is always pointing to the center of the Earth, the X axis follows the same path as the velocity vector of the satellite and the Y vector just the resultant of the natural vector product between the previous two. This system is illustrated below:

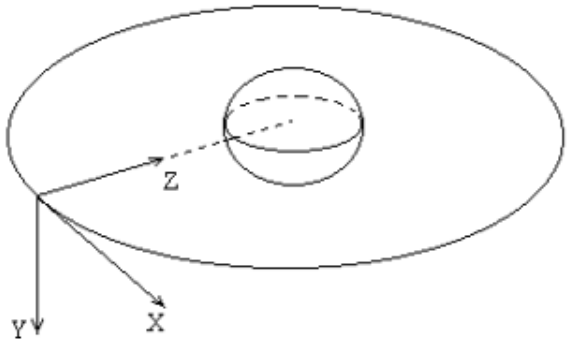

Fig. 3.2. Orbit-fixed Coordinate System

It should be noted that, as this system is rotating at a constant angular velocity, it is considered non-inertial. The unitary vectors are defined as $\vec{I}$, $\vec{J}$ and $\vec{K}$.

3.1.3. Body Fixed Coordinate System

This is the system used to project the equations of motion. The origin coincides with the center of mass of the satellite, the Z axis is aligned with the lowest moment of inertia and X and Y axes are aligned with the other two principal moments of inertia. The nominal conditions of this system match the orbit fixed system. The picture below shows the body fixed frame in a CubeSat 3U.

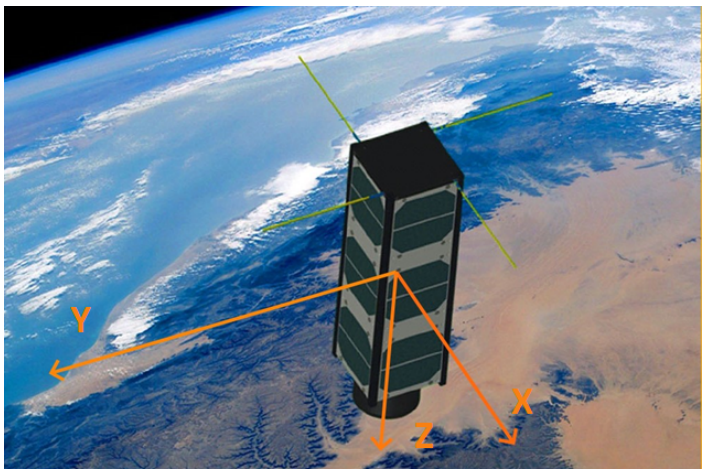

Fig. 3.3. Body Fixed Coordinate System

The unitary vectors of this coordinate system are $\vec{i}$, $\vec{j}$ and $\vec{k}$.

3.2. Attitude Representation

The attitude is defined as the orientation of the body fix frame with respect to the orbit-fixed one. For a proper parametrization the selected Euler sequence is 2-1-3 (Y-X-Z), also called *Tait-Bryan* or *Cardan* Angles. These rotations are physically represented below:

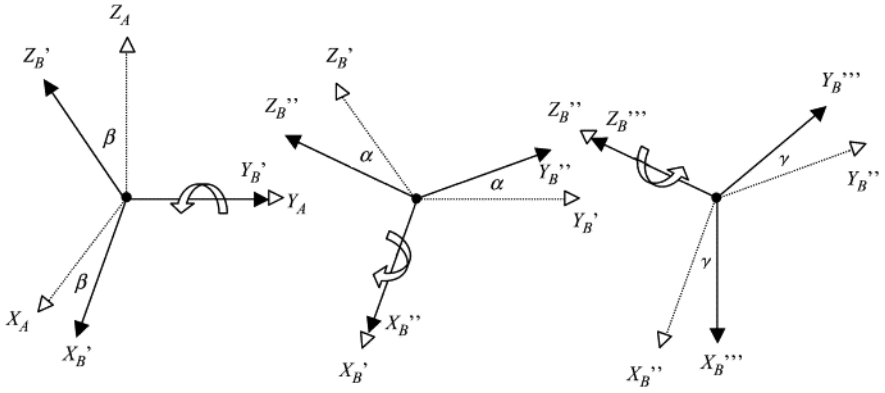

Fig. 3.4. Definition of the rotation sequence

The first rotation about the Y_A axis is represented by the angle β, the second one, about the intermediate axis X'_B, by the angle α and last one, about axis Z''_B by the angle γ. Note that the axes Y_A and Z''_B belong to the orbit fixed and body fixed frames respectively.

Now, the rotation matrix of the transformation needs to be obtained. This is simply done multiplying the matrices of each rotation sequence as follows:

$$\begin{bmatrix} \vec{i} \\ \vec{j} \\ \vec{k} \end{bmatrix} = \Big[R\Big] \begin{bmatrix} \vec{I} \\ \vec{J} \\ \vec{K} \end{bmatrix} \tag{3.1}$$

$$\begin{bmatrix} \vec{i} \\ \vec{j} \\ \vec{k} \end{bmatrix} = \Big[R(\gamma)\Big]\Big[R(\alpha)\Big]\Big[R(\beta)\Big] \begin{bmatrix} \vec{I} \\ \vec{J} \\ \vec{K} \end{bmatrix} \tag{3.2}$$

$$\begin{bmatrix} \vec{i} \\ \vec{j} \\ \vec{k} \end{bmatrix} = \begin{bmatrix} c(\gamma) & s(\gamma) & 0 \\ -s(\gamma) & c(\gamma) & 0 \\ 0 & 0 & 1 \end{bmatrix} \begin{bmatrix} 1 & 0 & 0 \\ 0 & c(\alpha) & s(\alpha) \\ 0 & -s(\alpha) & c(\alpha) \end{bmatrix} \begin{bmatrix} c(\beta) & 0 & -s(\beta) \\ 0) & 1 & 0 \\ s(\beta) & 0 & c(\beta) \end{bmatrix} \begin{bmatrix} \vec{I} \\ \vec{J} \\ \vec{K} \end{bmatrix} \tag{3.3}$$

So the matrix multiplication brings:

$$\Big[R\Big] = \begin{bmatrix} c(\gamma)c(\beta) + s(\gamma)s(\alpha)s(\beta) & s(\gamma)c(\alpha) & -s(\beta)c(\gamma) + s(\gamma)s(\alpha)c(\beta) \\ -s(\gamma)c(\beta) + c(\gamma)s(\alpha)s(\beta) & c(\gamma)c(\alpha) & s(\gamma)s(\beta) + c(\gamma)s(\alpha)c(\beta) \\ s(\beta)c(\alpha) & -s(\alpha) & c(\alpha)c(\beta) \end{bmatrix} \tag{3.4}$$

It should be noted that if the reverse operation wants to be performed, $BF_{axes} \rightarrow OF_{axes}$, it will be enough to calculate the inverse of the matrix 3.4

$$\begin{bmatrix} \vec{I} \\ \vec{J} \\ \vec{K} \end{bmatrix} = \Big[R\Big]^{-1} \begin{bmatrix} \vec{i} \\ \vec{j} \\ \vec{k} \end{bmatrix} \tag{3.5}$$

3.2.1. Quaternions

The representation of the attitude of an object, in this case the satellite, using Euler angles is simple to develop and visualize but it could imply a major drawback for some reasons. The first one, Euler angles are computationally more intense compared to quaternions and second and more important, the singularity problem that occurs with certain combinations that cause the famous *Gimbal Lock*.

The quaternion representation method is based on Euler's theorem which states that the relative orientation of two coordinate systems can be defined by only one rotation about a fixed axis. With this idea in mind, the implementation of the rotation kinematics is done using this number system.

A quick overview about quaternion operation will be done, showing the most important equations but in order to check more information about their properties and significance, please refer to [17] and [18].

The quaternion below represents a coordinate transformation between 2 systems

$$\vec{Q} = Q_s + Q_1\vec{i} + Q_2\vec{j} + Q_3\vec{k} \tag{3.6}$$

where the included vectors are unit vectors. The previous expression is mathematically equivalent to

$$\vec{Q} = \begin{bmatrix} Q_s \\ Q_1 \\ Q_2 \\ Q_3 \end{bmatrix} = \begin{bmatrix} cos(\frac{\theta}{2}) \\ ||\vec{e}||sin(\frac{\theta}{2}) \end{bmatrix} \tag{3.7}$$

where $||\vec{e}||$ is the normalized axis of rotation and θ is the transformation angle, the picture below explains this concept more clearly

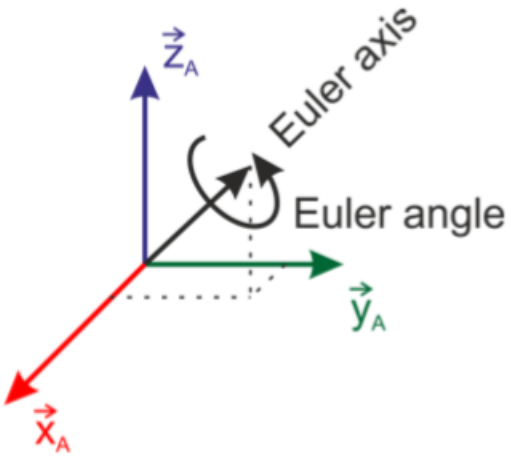

Fig. 3.5. Visual representation of Euler's rotational theorem

In order to obtain the quaternions from Euler angles, the little algorithm shown in [17] is used. Four initial values of the quaternion's components are obtained through the values of the rotational matrix 3.4 and implementing a short conditional statement the true values are defined.

Once the four values are set, the system of kinematic equations that relate the angular velocity and the quaternion with the derivative of the latter. It is a system of four first order ODEs in the form

$$\begin{bmatrix} \dot{Q}_1 \\ \dot{Q}_2 \\ \dot{Q}_3 \\ \dot{Q}_4 \end{bmatrix} = \frac{1}{2} \begin{bmatrix} 0 & -\omega_x & -\omega_y & -\omega_z \\ \omega_x & 0 & \omega_z & -\omega_y \\ \omega_y & -\omega_z & 0 & \omega_x \\ \omega_z & \omega_y & -\omega_x & 0 \end{bmatrix} \begin{bmatrix} Q_1 \\ Q_2 \\ Q_3 \\ Q_4 \end{bmatrix} \tag{3.8}$$

For the inverse operation, the equivalent of the rotational matrix defined in quaternion form is

$$\left[R_Q\right] = \begin{bmatrix} Q_1^2 + Q_2^2 - Q_3^2 - Q_4^2 & 2(Q_2Q_3 + Q_4Q_1) & 2(Q_2Q_4 - Q_3Q_1) \\ 2(Q_2Q_3 - Q_4Q_1) & Q_1^2 - Q_2^2 + Q_3^2 - Q_4^2 & 2(Q_3Q_4 + Q_2Q_1) \\ 2(Q_2Q_4 + Q_3Q_1) & 2(Q_3Q_4 - Q_2Q_1) & Q_1^2 - Q_2^2 - Q_3^2 + Q_4^2 \end{bmatrix} \tag{3.9}$$

and the corresponding Euler angles definitions are simply obtained from the relationship with the rotational matrix 3.4 as

$$\alpha = asin\Big(-R_{Q,32}\Big) \tag{3.10}$$

$$\beta = atan\left(\frac{R_{Q,31}}{R_{Q,33}}\right) \tag{3.11}$$

$$\gamma = atan\left(\frac{R_{Q,12}}{R_{Q,22}}\right) \tag{3.12}$$

Last but not least, an easy way to check if the quaternions are being calculated correctly, is to perform the squared sum of its components.

$$Q_1^2 + Q_2^2 + Q_3^2 + Q_4^2 = 1 \tag{3.13}$$

As they are normalized vectors, the theoretical sum of its components should be 1. This check is implemented in the code to monitor the error of the conversion.

3.3. Equations of Motion

The Euler equations of motion describe the rotation of a rigid body using a rotating reference frame with its axes fixed to the body and aligned to the body's principal axes of inertia. They have the form:

$$I_x\dot{\omega}_x + (I_z - I_y)\omega_y\omega_z = M_x \tag{3.14}$$

$$I_y\dot{\omega}_y + (I_x - I_z)\omega_x\omega_z = M_y \tag{3.15}$$

$$I_z\dot{\omega}_z + (I_y - I_x)\omega_x\omega_y = M_z \tag{3.16}$$

Where the angular velocity terms and their derivatives are written with respect to the inertial reference frame shown in section 3.1.1. The terms I_x, I_y and I_z are the principal axes of inertia and M_x, M_y and M_z the applied torques. All of them will be projected in body fixed coordinates.

3.3.1. Applied Torques

This work is focused on the disturbances occurring when the satellite is under the effect of the Earth's gravity gradient, hence, this torque will be the only one applied.

It is known that the point value of the gravity decreases with the square of the distance of that point to the center of the Earth. Being this satellite a slender body, the effect is quite important and should be carefully taken into account and later studied.

Starting with the description of the differential of the force, written

$$d\vec{F} = -\frac{\mu(\vec{R} + \vec{\rho})}{||\vec{R} + \vec{\rho}||^3}dm \tag{3.17}$$

Here, μ is the product of the universal gravitational constant and the mass of the Earth, adding up to $\mu = 3.9858 \cdot 10^{14}$. $\vec{R}$ is the vector of the center of mass of the satellite in orbit fixed frame and $\vec{\rho}$ is the vector of each differential of mass in body fixed axes. Integrating

$$\vec{M_{gg}} = -\mu \int_V \frac{\vec{\rho} \wedge \vec{R}}{||\vec{R} + \vec{\rho}||^3}dm \tag{3.18}$$

Expressing again each of the terms in body fixed frame

$$\vec{R}_{BF} = \begin{bmatrix} -R_{13}R \\ -R_{23}R \\ -R_{33}R \end{bmatrix} \tag{3.19}$$

$$\vec{\rho}_{BF} = \begin{bmatrix} x \\ y \\ z \end{bmatrix} \tag{3.20}$$

To avoid any confusion, it should be remarked the differences between the term R referring to the position of the center of mass of the satellite and R_{ij}, being i the row position and j the column position, referring to each of the terms of the rotational matrix described in equation 3.4.

Assuming that $\rho << R$, the denominator is simplified as

$$\|\vec{R_{BF}} + \vec{\rho_{BF}}\|^3 \approx \frac{1}{R^3}\left(1 + 3\frac{R_{13}x + R_{23}y + R_{33}z}{R}\right) \tag{3.21}$$

substituting in 3.18, it leads to

$$\vec{M}_{gg,BF} = -3\frac{\mu}{R^3}\begin{bmatrix} R_{23}R_{33}(I_y - I_z) \\ R_{13}R_{33}(I_z - I_x) \\ R_{13}R_{23}(I_x - I_y) \end{bmatrix} \tag{3.22}$$

and knowing that the satellite's orbit is perfectly circular, its orbit's angular velocity is $\Omega = \sqrt{\frac{\mu}{R^3}}$, the final expression for the gravity gradient torque is

$$\vec{M}_{gg,BF} = -3\Omega^2\begin{bmatrix} R_{23}R_{33}(I_y - I_z) \\ R_{13}R_{33}(I_z - I_x) \\ R_{13}R_{23}(I_x - I_y) \end{bmatrix} \tag{3.23}$$

3.3.2. Angular velocity

As it was said before, the Euler equations will be projected in body axes, so do the angular velocity.

The expression of the angular velocity of the satellite with respect to the inertial system of section 3.1.1 is

$$\vec{\omega_0} = \vec{\Omega_0} + \vec{\omega_{BF}} \tag{3.24}$$

The transformation of $\vec{\omega_0}$ to body axes has to be done in 2 steps, first to orbit fixed

$$\vec{\Omega_0} = -\Omega\vec{J} \tag{3.25}$$

and second, to body fixed

$$\Omega\vec{J} = \begin{bmatrix} \Omega R_{12}\vec{i} \\ \Omega R_{22}\vec{j} \\ \Omega R_{32}\vec{k} \end{bmatrix} \tag{3.26}$$

For the angular velocity of the satellite with respect to orbit fixed axes, using the notation of 3.4 as follows:

$$\vec{\omega_{BF}} = \dot{\beta}\vec{J} + \dot{\alpha}\vec{X'_B} + \dot{\gamma}\vec{j} \tag{3.27}$$

the expression of $\vec{\omega_{BF}}$, applying the vector transformation for $\vec{J}$ and $\vec{X'_B}$ results

$$\vec{\omega_{BF}} = \begin{bmatrix} p \\ q \\ r \end{bmatrix} = \begin{bmatrix} \dot{\beta}cos(\alpha)sin(\gamma) + \dot{\alpha}cos(\gamma) \\ \dot{\beta}cos(\alpha)cos(\gamma) - \dot{\alpha}sin(\gamma) \\ \dot{\gamma} - \dot{\beta}sin(\alpha) \end{bmatrix} \tag{3.28}$$

so the final expression of the angular velocity $\vec{\omega_0}$ and its derivative in body fixed frame is:

$$\omega_x = p - \Omega R_{12} \qquad \dot{\omega_x} = \dot{p} - \Omega \dot{R_{12}} \tag{3.29}$$

$$\omega_y = q - \Omega R_{22} \qquad \dot{\omega_y} = \dot{q} - \Omega \dot{R_{22}} \tag{3.30}$$

$$\omega_z = r - \Omega R_{32} \qquad \dot{\omega_z} = \dot{r} - \Omega \dot{R_{32}} \tag{3.31}$$

It is very important to remark that the Coriolis terms of the derivatives have been canceled due to the definition of a derivative of a vector with respect to a non-inertial reference frame. *Coriolis' theorem* states that the derivative of a vector in a non-inertial reference frame is given by the derivative of its components as seen by the rotating frame, plus an additional term given by the vector product between the angular velocity of the rotating frame and the vector itself. As it is shown below the components of the vector product are exactly the same, so the second term below is cancelled.

$$\frac{d\vec{\omega_0}}{dt} = \left[\frac{d\vec{\omega_0}}{dt}\right]_{BF} + \cancel{\vec{\omega_0} \wedge \vec{\omega_0}} = \left[\frac{d\vec{\omega_0}}{dt}\right]_{BF} \tag{3.32}$$

3.4. Final expression of Euler Equations

Substituting all the previous terms into equations 3.14, 3.15 and 3.16, the final set of equations of motion are read

$$I_x\dot{p} + (I_z - I_y)qr - I_x\Omega\dot{R_{12}} - (I_z - I_y)(\Omega qR_{32} + \Omega rR_{22}) + R_{32}R_{22}\Omega^2(I_z - I_y) = -3\Omega^2 R_{23}R_{33}(I_y - I_z) \tag{3.33}$$

$$I_y\dot{q} + (I_x - I_z)pr - I_y\Omega\dot{R_{22}} - (I_x - I_z)(\Omega pR_{32} + \Omega rR_{12}) + R_{12}R_{32}\Omega^2(I_x - I_z) = -3\Omega^2 R_{13}R_{33}(I_y - I_z) \tag{3.34}$$

$$I_z\dot{r} + (I_y - I_x)pq - I_z\Omega\dot{R_{32}} - (I_y - I_x)(\Omega qR_{12} + \Omega pR_{22}) + R_{12}R_{22}\Omega^2(I_y - I_x) = -3\Omega^2 R_{13}R_{23}(I_y - I_z) \tag{3.35}$$

and the only terms that have not been defined are the derivatives of the rotation matrix components

$$\dot{R_{12}} = -\dot{\alpha}sin(\alpha)sin(\gamma) + \dot{\gamma}cos(\alpha)cos(\gamma) \tag{3.36}$$

$$\dot{R_{22}} = -\dot{\alpha}sin(\alpha)cos(\gamma) - \dot{\gamma}cos(\alpha)sin(\gamma) \tag{3.37}$$

$$\dot{R_{32}} = -\dot{\alpha}cos(\alpha) \tag{3.38}$$

The integration of the first order ODEs 3.33, 3.34 and 3.35 together with kinematic equations in quaternion form 3.8 is performed via *Simulink* (MATLAB), applying the numerical methods that *ode*45 typically uses. *Simulink* integrators have as inputs a set of 6 initial conditions

$$\dot{\vec{I.C}} = \begin{bmatrix} \alpha_0 \\ \beta_0 \\ \gamma_0 \\ p_0 \\ q_0 \\ r_0 \end{bmatrix} \tag{3.39}$$

3.5. Linearization and analytical solution

In order to create a functional algorithm, it is necessary to obtain the simplified analytical solution of the previously defined non-linear Euler equations. As the previous development, this will be done by means of [16].

3.5.1. Linearization

The main hypothesis proposed to linearize the equations is within the description of the problem. As this work is exclusively focus on the small perturbations from the satellite's nominal position due to the gravity gradient and the slender body condition, the assumption of small *roll* and *pitch* angles ($\alpha, \beta \ll 1$) is expected to bring accurate results.

In principle, the angular velocity r or *spin* is not negligible and in fact, will be much larger than the orbit's angular velocity Ω. This condition will cause the angle γ to reach any value from 0 to 2π. However, in the following pages, a way to linearize the *yaw* angle is introduced as well.

Linearization of the equations follows these assumptions:

- $\sin(\alpha)$, $\sin(\beta) \approx \alpha, \beta$
- $\cos(\alpha)$, $\cos(\beta) \approx 1, 1$
- $\sin(\alpha) \cdot \sin(\beta) \approx 0$

- $\dot{\alpha} \cdot \dot{\beta} \approx 0$

And applying one the very first conditions stated in chapter **??**, $I_x = I_y$, the following set of linearized equations is

$$I_x(\ddot{\beta}sin\gamma+\ddot{\alpha}cos\gamma)+I_z\dot{\beta}\dot{\gamma}cos\gamma-I_z\dot{\alpha}\dot{\gamma}sin\gamma = 4\Omega^2(I_z-I_x)\alpha cos\gamma+I_z\Omega\dot{\gamma}cos\gamma+3\Omega^2(I_z-I_x)\beta sin\gamma \tag{3.40}$$

$$I_x(\ddot{\beta}cos\gamma-\ddot{\alpha}sin\gamma)-I_z\dot{\beta}\dot{\gamma}sin\gamma-I_z\dot{\alpha}\dot{\gamma}cos\gamma = -4\Omega^2(I_z-I_x)\alpha sin\gamma-I_z\Omega\dot{\gamma}sin\gamma+3\Omega^2(I_z-I_x)\beta cos\gamma \tag{3.41}$$

$$\ddot{\gamma} = -\Omega\dot{\alpha} \tag{3.42}$$

This system of equations is further simplified substituting eqs 3.40 and 3.41 by a linear combination of both, resulting in

$$I_x\ddot{\beta} - I_z\dot{\alpha}\dot{\gamma} + 3\Omega^2(I_x - I_z)\beta = 0 \tag{3.43}$$

$$I_x\ddot{\alpha} + I_z\dot{\beta}\dot{\gamma} + 4\Omega^2(I_x - I_z)\alpha - I_z\Omega\dot{\gamma} = 0 \tag{3.44}$$

Following as well the idea of [16], γ was not able to be linearized due to its full range of values. Nonetheless, taking advantage of the fact of a high *spin* velocity in comparison with Ω, from now on, the *spin* will be denoted by w_s.

The procedure shows that the *yaw* angle can be decomposed as the sum of a big term and a small one

$$\gamma = w_s t + \delta \tag{3.45}$$

with $\delta \ll w_s t$. Then we take derivatives of equation 3.45

$$\dot{\gamma} = w_s + \dot{\delta} \tag{3.46}$$

$$\ddot{\gamma} = \ddot{\delta} \tag{3.47}$$

and substituting in 3.42

$$\ddot{\delta} = -\Omega\dot{\alpha} \tag{3.48}$$

and integrating again once,

$$\dot{\delta} = -\Omega\alpha + \Omega\alpha_0 \tag{3.49}$$

substituting equations 3.46 and 3.49 into 3.43 and 3.44 and neglecting second order terms again, the equations become

$$I_x\ddot{\beta} - I_z\dot{\alpha}w_s + 3\Omega^2(I_x - I_z)\beta = 0 \tag{3.50}$$

$$I_x\ddot{\alpha} + I_z\dot{\beta}w_s + 4\Omega^2\left(I_x - \frac{3}{4}I_z\right)\alpha - I_z\Omega w_s = 0 \tag{3.51}$$

$$\dot{\delta} = -\Omega\alpha + \Omega\alpha_0 \tag{3.52}$$

The very last step before starting to discuss it analytically is to adimensionalize it. The following adimensional parameters are defined:

$$I = \frac{I_z}{I_x}$$

$$\tilde{\omega} = \frac{w_s}{\Omega}$$

$$\tau = \Omega t$$

and dividing the first two equations by Ω^2 and I_x and the last one just by Ω, the final adimensional linearized equations are

$$\beta'' - I\alpha'\tilde{\omega} + 3(1 - I)\beta = 0 \tag{3.53}$$

$$\alpha'' + I\beta'\tilde{\omega} + 4\left(1 - \frac{3}{4}I\right)\alpha - I\tilde{\omega} = 0 \tag{3.54}$$

$$\delta' = -\alpha + \alpha_0 \tag{3.55}$$

3.5.2. Analytical Solution

It can be seen that the first two equations 3.53 and 3.54 are decoupled from the third one. So the system can be solved using the first two equations and then apply the results to the third one in order to obtain the third angle.

The whole process to obtain the solution does not present much complexity but it could result long and tedious. For those interested, the full development is found again within article [16].

The important points to take into account in order to correctly study the behavior in time of the system start with the particular solutions of equations 3.53 and 3.54,

$$\beta_P = 0 \tag{3.56}$$

$$\alpha_P = \tilde{\omega}\frac{I}{4 - 3I} \tag{3.57}$$

The particular solution α_P is also called *Roll-bias*. Applying the condition of slender body $I \ll 1$, automatically, $\alpha_P \ll 1$

From the characteristic equation of the system,

$$\sigma^4 + (7 - 6I + I^2\tilde{\omega}^2)\sigma^2 + 3(1 - I)(4 - 3I) = 0 \tag{3.58}$$

the frequencies σ_i are calculated

$$\sigma_{1,3} \approx \pm 2i \tag{3.59}$$

$$\sigma_{2,4} \approx \pm \sqrt{3}i \tag{3.60}$$

It can be seen that both frequencies are pure frequencies (no real part) but slightly different in value. It is determined that the system is *stable* as long as the condition $I \ll 1$ remains, independently of the value of the adimensional spin $\tilde{\omega}$

Finally the analytical solution of the system is

$$\alpha = C_1 S_{21} cos\sigma_1\tau + C_2 T_{21} sin\sigma_1\tau + C_3 S_{22} cos\sigma_2\tau + C_4 T_{22} sin\sigma_2\tau + \tilde{\omega}\frac{I}{4 - 3I} \tag{3.61}$$

$$\beta = C_1 S_{11} cos\sigma_1\tau + C_2 T_{11} sin\sigma_1\tau + C_3 S_{12} cos\sigma_2\tau + C_4 T_{12} sin\sigma_2\tau \tag{3.62}$$

$$\delta = C_1\left(-\frac{S_{21}}{\sigma_1}\right)sin\sigma_1\tau + C_2\left(\frac{T_{21}}{\sigma_1}\right)cos\sigma_1\tau + C_3\left(-\frac{S_{22}}{\sigma_2}\right)sin\sigma_2\tau + C_4\left(\frac{T_{22}}{\sigma_2}\right)cos\sigma_2\tau - \tilde{\omega}\frac{I}{4 - 3I}\tau + \alpha_0\tau \tag{3.63}$$

Only the imaginary part of σ_i is taken in order to solve the equations. Moreover, T_{ij} and S_{ij} are defined as

$$S_{ij} = Re[a_{ij}] + Im[a_{ij}] \tag{3.64}$$

$$T_{ij} = Re[a_{ij}] - Im[a_{ij}] \tag{3.65}$$

and being a_{ij} the eigenvectors of the problem, whose value has been approximated following the assumptions to

$$\begin{bmatrix} a_{11} \\ a_{21} \end{bmatrix} = \begin{bmatrix} \frac{\sqrt{1-I-I^2\tilde{\omega}^2}}{\sqrt{3}I\tilde{\omega}}i \\ 1 \end{bmatrix} \tag{3.66}$$

$$\begin{bmatrix} a_{12} \\ a_{22} \end{bmatrix} = \begin{bmatrix} 1 \\ \frac{\sqrt{1-0.75I+I^2\tilde{\omega}^2}}{2I\tilde{\omega}}i \end{bmatrix} \tag{3.67}$$

and last, the constants C_1, C_2, C_3 and C_4 which depend on the initial conditions $\alpha_0, \beta_0, \dot{\alpha_0}$ and $\dot{\beta_0}$

$$C_3 = \frac{\beta_0 S_{21} - \alpha_0 S_{11} + \alpha_P S_{11}}{S_{12}S_{21} - S_{22}S_{11}} \tag{3.68}$$

$$C_1 = \frac{\beta_0 - C_3 S_{12}}{S_{11}} \tag{3.69}$$

$$C_4 = \frac{\dot{\beta}_0 T_{21} - \dot{\alpha}_0 T_{11}}{\sigma_2 (T_{12} T_{21} - T_{22} T_{11})} \tag{3.70}$$

$$C_2 = \frac{\dot{\beta}_0 - C_4 T_{12} \sigma_2}{\sigma_1 T_{11}} \tag{3.71}$$

3.6. Horizon Sensor angles

Once the analytical solution is ready to be implemented, the last part before developing the algorithm is to extract the horizon sensor angles. This will be done introducing the Euler angles obtained from the simulation in the equations that will be deduced below.

The orientation angle of the cameras within the horizon sensors is chosen solving the following simple trigonometric problem,

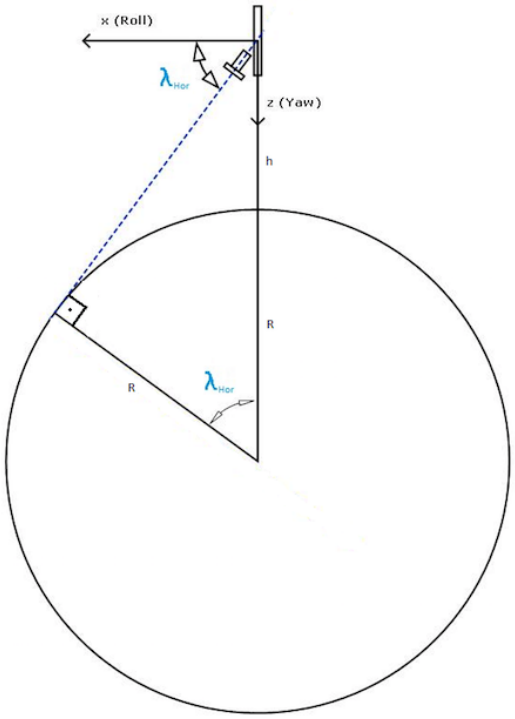

Fig. 3.6. HS Camera's orientation angle

From there, using the particular data of the mission, the angle is obtained

$$\lambda_{hor} = acos\left(\frac{R_{Earth}}{R_{Earth} + h_{sat}}\right) \approx 30.05^{o} \tag{3.72}$$

From figure 3.6 the orientation of horizon vector explained in chapter **??** is defined.

Following the guidelines of [15] but applying some changes in the orientation of the reference frames shown in the document, the system of equations that provide the horizon sensor angles are going to be deduced. Before doing so, in order to provide a proper visualization of the problem. Using the information of chapter **??**, the following pair of schemes, showing the orbit fixed and body fixed coordinate systems as well as the direction vector of the cameras. The sketch made for the first camera, or cam-1,

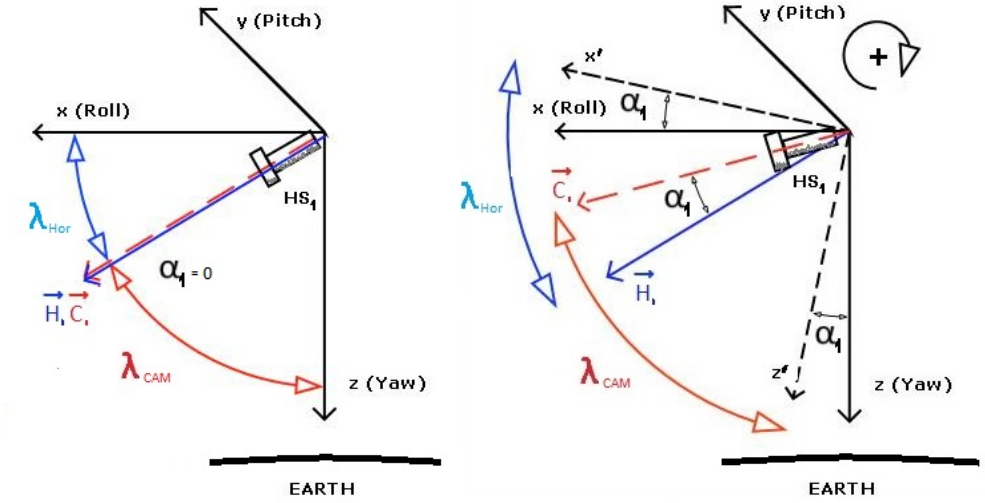

(a) cam-1 initial position for $\beta_0 = 0$ (b) cam-1 initial position for $\beta_0 \neq 0$

Fig. 3.7. Sketch of the positioning of the first camera

and for the second camera, or cam-2,

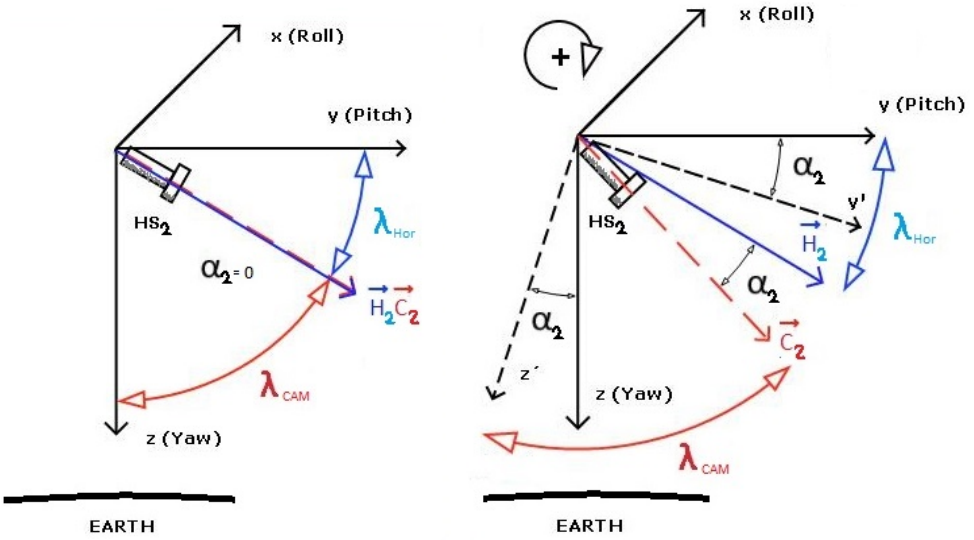

(a) cam-2 initial position for $\alpha_0 = 0$ (b) cam-2 initial position for $\alpha_0 \neq 0$

Fig. 3.8. Sketch of the positioning of the second camera

By definition, the angle λ_{cam} is fixed and it reads

$$\lambda_{cam} = \frac{\pi}{2} - \lambda_{hor} \tag{3.73}$$

Once the problem is visualized, it is not complex to obtain the equations relating the camera angles and the Euler angles. Taking into account the definition of the horizon vectors $\vec{H_1}$ and $\vec{H_2}$ from figures 3.7 and 3.8. Expressed in body fixed frame,

$$\vec{H_1} = sin(\lambda_{cam} - \alpha_1)\vec{i} + 0\vec{j} + cos(\lambda_{cam} - \alpha_1)\vec{k} \tag{3.74}$$

$$\vec{H_2} = 0\vec{i} + sin(\lambda_{cam} - \alpha_2)\vec{j} + cos(\lambda_{cam} - \alpha_2)\vec{k} \tag{3.75}$$

Equations 3.74 and 3.75 show that α_1, the angle swept by cam-1 is positive when β_0 is also positive. However, the sense of rotation of the *roll* axis will bring a negative cam-2 angle when $\alpha_0 > 0$

Now, the rotation matrix 3.4 is used to transform the horizon vectors to orbit fixed frame as,

$$\begin{bmatrix} H_{1,x} \\ H_{1,y} \\ H_{1,z} \end{bmatrix}_{OF} = \Big[R\Big]^{-1} \begin{bmatrix} h_{1,x} \\ h_{1,y} \\ h_{1,z} \end{bmatrix}_{BF} \tag{3.76}$$

$$\begin{bmatrix} H_{2,x} \\ H_{2,y} \\ H_{2,z} \end{bmatrix}_{OF} = \Big[R\Big]^{-1} \begin{bmatrix} h_{2,x} \\ h_{2,y} \\ h_{2,z} \end{bmatrix}_{BF} \tag{3.77}$$

The last components of each of the vectors calculated, $H_{1,z}$ and $H_{2,z}$ are known (they are the same indeed $H_{1,z} = H_{2,z}$), so their two expressions are formulated as follows

$$R_{13}sin(\lambda_{cam} - \alpha_1) + R_{33}cos(\lambda_{cam} - \alpha_1) = H_{1,z} \approx sin(30.05) \tag{3.78}$$

$$R_{23}sin(\lambda_{cam} - \alpha_2) + R_{33}cos(\lambda_{cam} - \alpha_2) = H_{2,z} \approx sin(30.05) \tag{3.79}$$

Using some trigonometric identities (angle difference and pythagorean) a set of two quadratic equations is obtained, ready to be solved,

$$(A^2 + B^2)sin\alpha_1{}^2 - 2AH_{1,z}sin\alpha_1 + (H_{1,z}^2 - B^2) = 0 \tag{3.80}$$

$$(A_2{}^2 + B^2)sin\alpha_2{}^2 - 2A_2H_{2,z}sin\alpha_2 + (H_{2,z}^2 - B^2) = 0 \tag{3.81}$$

where the terms A, A_2 and B are defined as

$$A = R_{13} sin\lambda_{cam} + R_{33} cos\lambda_{cam} \tag{3.82}$$

$$A_2 = R_{23} sin\lambda_{cam} + R_{33} cos\lambda_{cam} \tag{3.83}$$

$$B = R_{33} \tag{3.84}$$

With this solution, the camera angles can be obtained using the data coming from the simulation, that is to say, the horizon sensor data received is simulated *real time*

3.7. Optimization algorithm

Once the Analytical solution and the cam angles are defined, the last step is to design the algorithm itself. As the satellite is only able to use the data coming from the horizon sensor, the main goal is to replicate that signal as accurately as possible.

In section 3.6 it is shown how to obtain the angles of the cameras from the simulated attitude of the satellite and section 3.5.2 describes the analytical solution of the linearized equations. This means that giving values to the four free constants and the adimensional *spin* defined in 3.5.2 will provide values for the Euler angles, which in turn will also give those of the cameras (α_1 and α_2)

In order to replicate the real signal coming from the cameras, the Mean Squared Error of the two camera angles together will be minimized. The Mean Square Error or Mean Quadratic Error evaluates the quality of a predictor. It measures the degree of dispersion of the predicted data, which in this case are the camera angles obtained from the Euler equations. The formula of the Mean Square Error of the predicted camera angles is,

$$MSE_{cams} = \frac{1}{n}\sum_{i=1}^{n}(\alpha_{1,real,i} - \alpha_{1,pred,i})^2 + \frac{1}{n}\sum_{i=1}^{n}(\alpha_{2,real,i} - \alpha_{2,pred,i})^2 \tag{3.85}$$

and writing it in the form of a scalar function

$$MSE_{cams} = f(\alpha_0, \beta_0, \dot{\alpha_0}, \dot{\beta_0}) \tag{3.86}$$

It should be noted that the satellite is assumed to be equipped with a device able to calculate and provide true values of the spin angular velocity $\tilde{\omega}$ so it will be included as a parameter in the algorithm.

The last step of the algorithm is to retrieve values of the selected constants that minimize the function MSE_{cams}. In order to do so, the selected built-in function MATLAB's *fminsearch*, is implemented using as inputs the function MSE_{cams} and the vector of initial guesses.

Besides, the tolerance was set to $tol = 10^{-11}$ and the number of iterations to 800.

The extended description of the algorithm that *fminsearch* has implemented can be found on [19] as it uses the *Nelder-Mead Method*.

3.7.1. Limitations

The *real* algorithm must be programmed to input a set of initial guesses that cover the spectrum where the solution is contained. This could result computationally dense depending on the equipment used to perform the calculations. In this work, the initial guesses were always input close to the real values. However, in the chapter 4 it is shown that depending on the real attitude of the satellite, it is possible to have a closer guess by inspecting the camera angles.

4. RESULTS

In this section, the results of the numerical integration, the analytical solution and the algorithm implementation mentioned in section **??** are presented, analyzed and interpreted. First, the model with no torques applied will be subtly commented. Afterwards, a comparison between the nonlinear simulation and the analytical solution (linearized system) will be done, studying the pros and cons of the linear theory applied. Third, the turn for the angles extracted from the camera equations; the variations in function of the $\tilde{\omega}$ and the initial conditions stated in 3.5.2. Fourth, will be the turn for the results of applying the algorithm in different scenarios, again varying the $\tilde{\omega}$ and the initial conditions. Last but not least, it is shown how the minimum Mean Squared Error varies in function of both the range of integration time span and fixed step size.

4.1. Free torque motion

The first step to validate the code is to test it in the free torque model. The equations governing the motion are seven, three related to the angular momentum of the system (Euler equations) and four kinematic equations in quaternion form. The third Euler equation is decoupled from the other two and its solution is a constant, the value of the initial condition, $r_0 = 3$ as it can be seen in figure 4.1

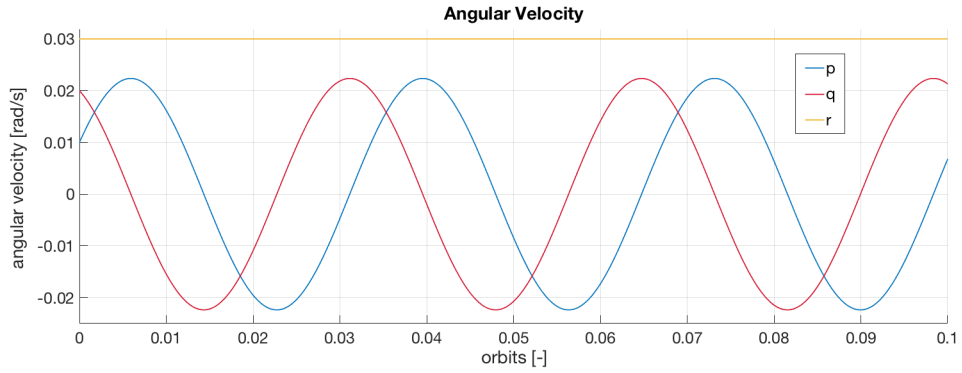

Fig. 4.1. angular velocity in free torque motion

The other two Euler equations form a simple system of two first order ordinary differential equations (ODEs) and as the solution of the third equation is a constant, the system can be converted to an equivalent scenario with two independent second order ODEs, which have an oscillatory solution which differ in phase, due to initial conditions. This can be seen as well in figure 4.1.

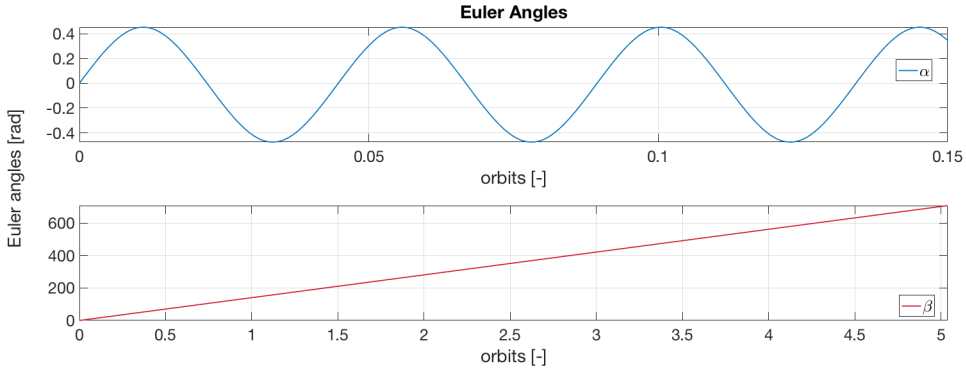

Fig. 4.2. Euler angles α and β in free torque motion

The two solutions for p and q oscillate harmonically about zero and their maximum and minimum values reach little over 0.02 and -0.02.

Concerning the attitude, the quaternion kinematics and afterwards their conversion to Euler angles through equations 3.10, 3.11 and 3.12 bring a linear solution for angle β, which infinitely increases at a considerable rate of $\approx$ 28.64 revs/orbit. α, however, has an oscillatory solution. Reaching values of ± 0.4 *rad*. This behavior can be explained analyzing the kinematic equations in Euler form, extracted from the inverse of matrix 3.28.

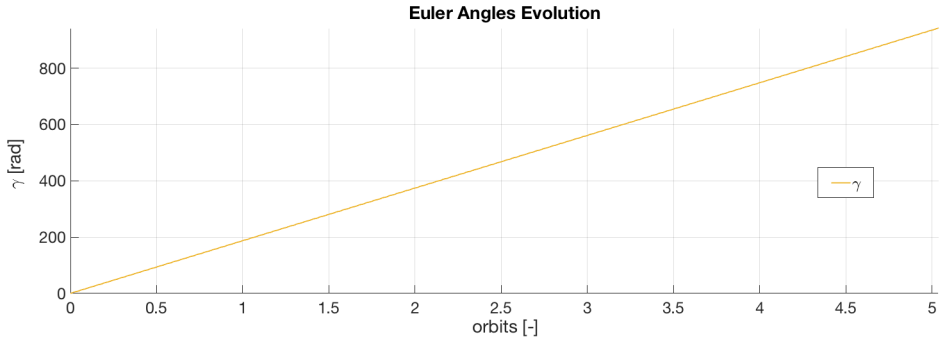

Fig. 4.3. γ angle in free torque motion

The yaw angle γ, follows the same behavior as the angle β, which a slightly larger slope.

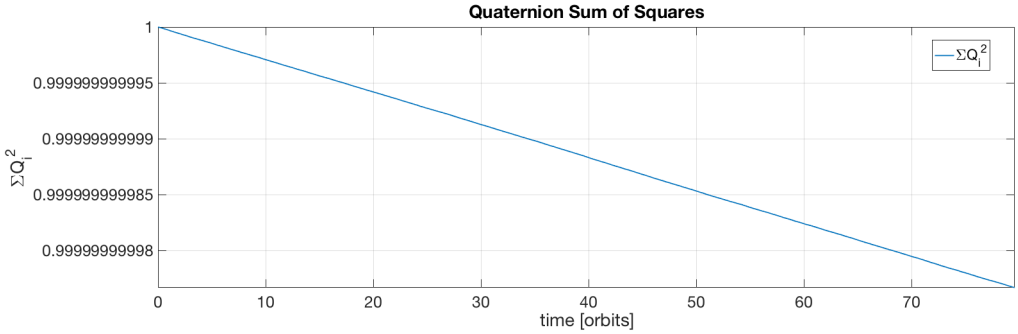

Fig. 4.4. quaternion transformation check in free torque motion

Finally, two quantities were calculated in order to help validating the code. The first one, following the equation 3.13, the quaternion components square sum result is found above. The error obtained is of the order of $10^{-}14$ which is highly accurate.

Second, the kinetic energy of the system was calculated following the simple equation

$$K_{en} = \frac{1}{2}(I_x p^2 + I_y q^2 + I_z r^2) + \frac{1}{2} M_{Sat} v_{Sat}^2 \tag{4.1}$$

As no torques are applied, theoretically the rotational kinetic energy must be conserved as the potential energy is zero. Figure 4.5 proves it,

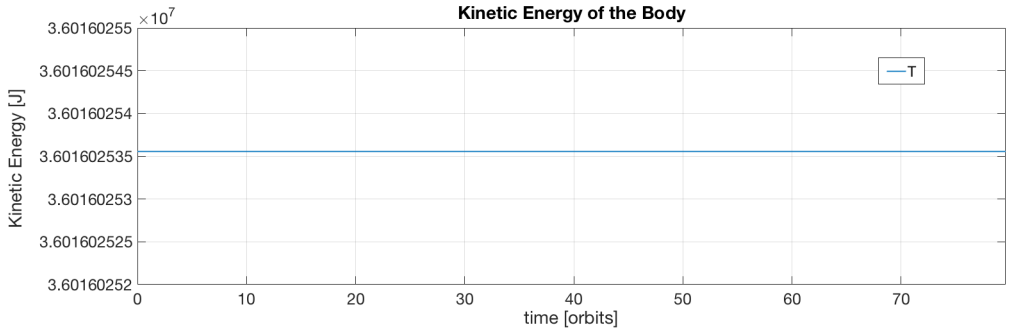

Fig. 4.5. kinetic energy of the body in free torque motion

4.2. Nonlinear-linear system comparison

In this section, the results obtained from the numerical integration of the complete nonlinear model and the solution of the analytical equation are compared. The aim is to analyze how effective and accurate the linear theory can be. Results for the analytical equations are retrieved by inputting the exact same initial conditions as the nonlinear model ($\alpha_0, \beta_0, \dot{\alpha_0}, \dot{\beta_0}$) plus the additional parameter $\tilde{\omega}$, which is set to different values in order to show the gyroscopic effects.

The following set of graphs will only show the orientation (attitude) of the satellite, this is to say, the Euler angles.

The first case, pictured in figures 4.6 and 4.7, shows the oscillation of Euler angles α, β and the small perturbation of the yaw angle, δ, which was completely defined in section 3.5.2.

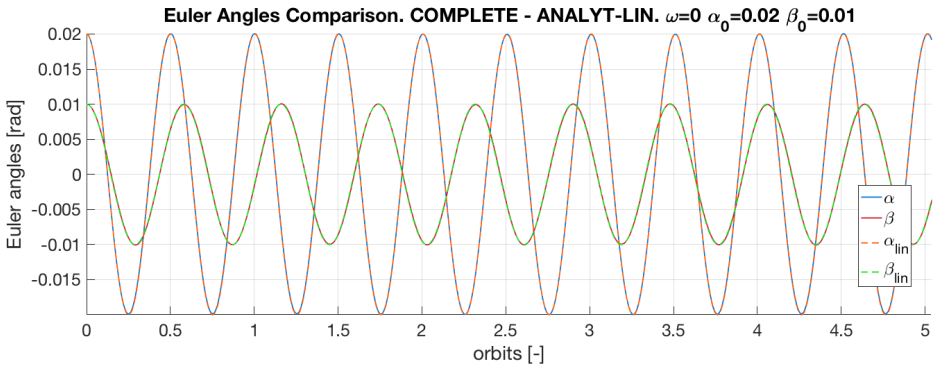

Fig. 4.6. α and β angles for $\tilde{\omega}$=0

The results show a perfect match between the nonlinear and the linear solution. Both α and β solutions show a perfectly harmonic oscillation with constant amplitude and frequency. Besides, as α_0 has a value two times larger compared to β_0 this results in a x2 larger amplitude as well. Moreover, the frequency of the angle β is clearly a little bit lower than α. This will bring different results as the $\tilde{\omega}$ starts increasing.

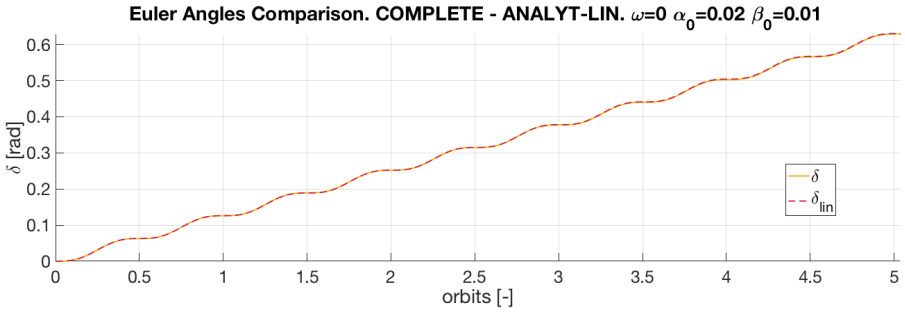

Fig. 4.7. δ perturbation for $\tilde{\omega}$=0

The yaw perturbation, δ is perfectly matched by the linear solution as well, as it was expected due to its linkage with the value of the angle α. Small oscillations about a line of slope=α_0 are obtained.

In the next scenario, the adimensional spin was set to $\tilde{\omega}$=10, maintaining the same initial conditions as before. It can be seen that β behaves almost identically as in the previous case, but showing little perturbations in amplitude. α has change its oscillation point due to the new value of the particular solution of the system of equations developed in section 3.5.2, where it was shown that the particular solution, α_P and also called *Roll bias* was uniquely dependant on the value of the $\tilde{\omega}$ and the adimensional moment of inertia I. As the latter was fixed by the mission, the new value of the particular solution is $\alpha_P \approx 0.0209$.

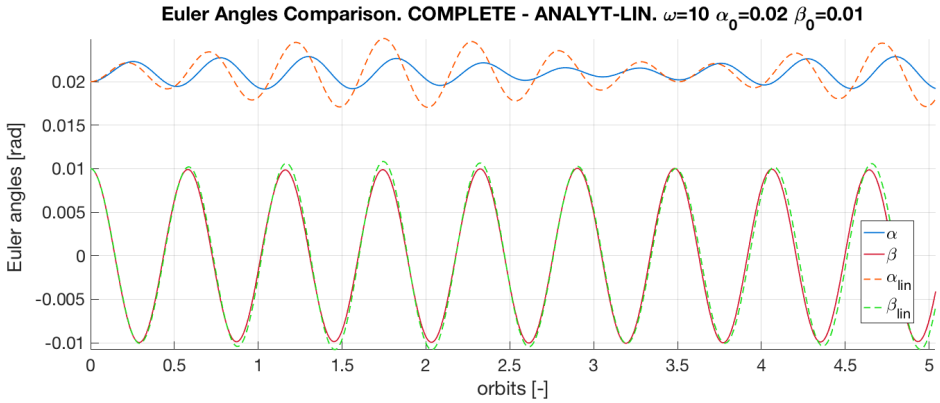

Fig. 4.8. α and β angles for $\tilde{\omega}$=10 and non zero IC

The previous statement can be visualized in figure 4.8. as the angle β oscillates near 0.021. Another phenomenon that is particular of soft coupled oscillators is the beat frequency waves or also called *beating*. This is present in angle α as well, where the oscillations change in amplitude like the effect of summing two frequencies at maximum amplitude point and cancelling frequencies at its minimum. As it was expected, the limitations of linear theory is starting to appear. The solution obtained for the angle α differs subtly from the nonlinear solution, specially in amplitude.

For the δ perturbation, one can find below,

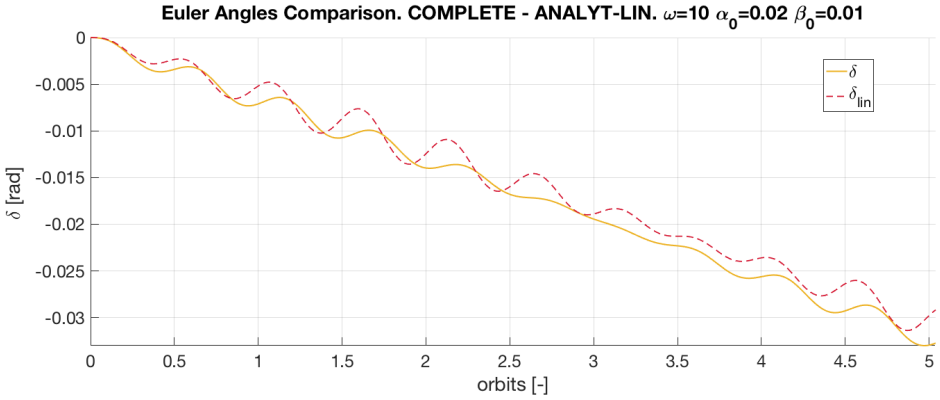

Fig. 4.9. δ perturbation for $\tilde{\omega}$=10 and non zero IC

As some error is obtained in the analytical solution of α, so does for δ. However, it can be seen that the slope is practically the same.

Now, the same scenario but starting from zero initial conditions. In this case a different order of magnitude is found for the values of α and β. As alpha is oscillating about the *roll-bias* it produces oscillations of one degree magnitude larger than β. These oscillations will start oscillations in β too, as it starts from zero, that is the reason why the linear theory shows more error in predicting angle β for this particular case. Additionally, it can be noted the previously defined effect of *beating* in β. Figure 4.10 shows this effect.

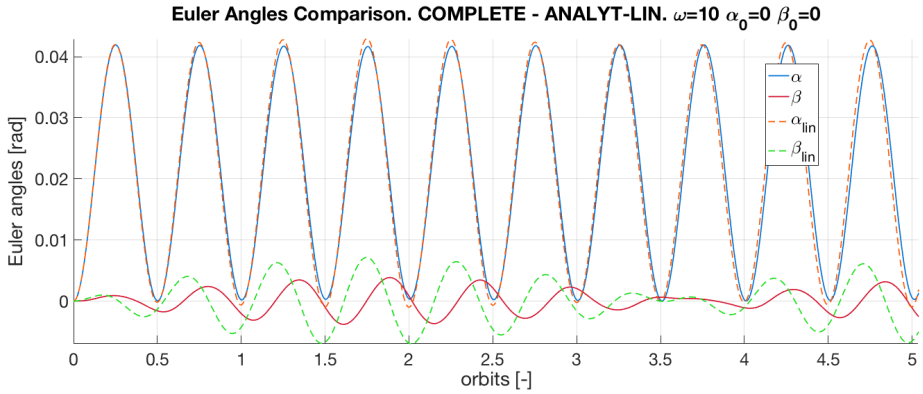

Fig. 4.10. α and β angles for $\tilde{\omega}$=10 and zero IC

The δ perturbation is almost perfectly matched by the linear theory as it was done with the α angle.

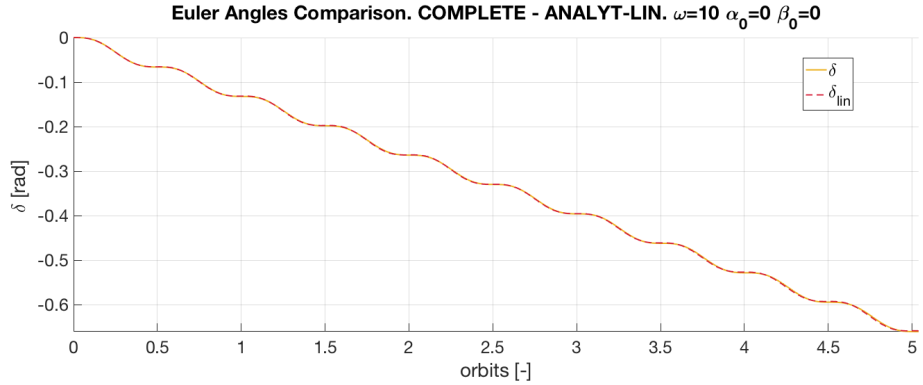

Fig. 4.11. δ perturbation for $\tilde{\omega}$=10 and zero IC

The last scenario was chosen in order to see the instabilities caused in the prediction of the Euler angles when a very high spin velocity is set, $\tilde{\omega} = 30$. The gyroscopic effects are much more visible in the figures below 4.12, 4.13.

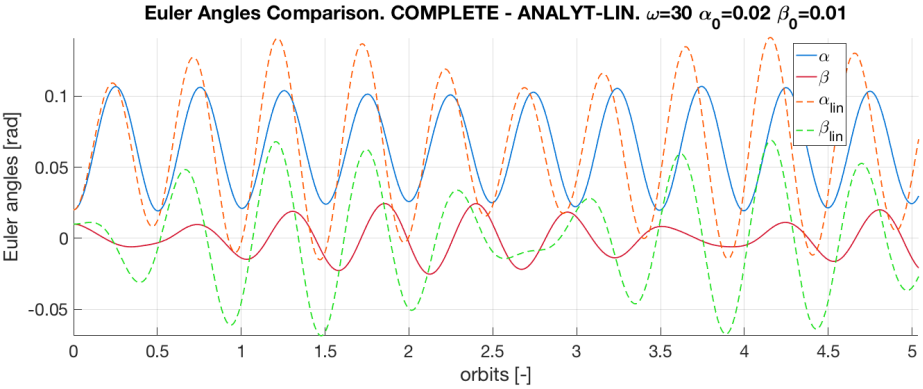

Fig. 4.12. α and β angles for $\tilde{\omega}$=30 and non zero IC

While the real signal coming from α is slightly damped, the linear results show a higher

amplitude variations, but these are not intense as the ones of β. In general as integration time passes, both linear solutions tend to develop a phase with respect to the nonlinear solution. This fact makes the accuracy of the analytical solution to be limited to small values of *spin*.

Results show that δ analytical is quite accurate compared to the rest of the Euler angles.

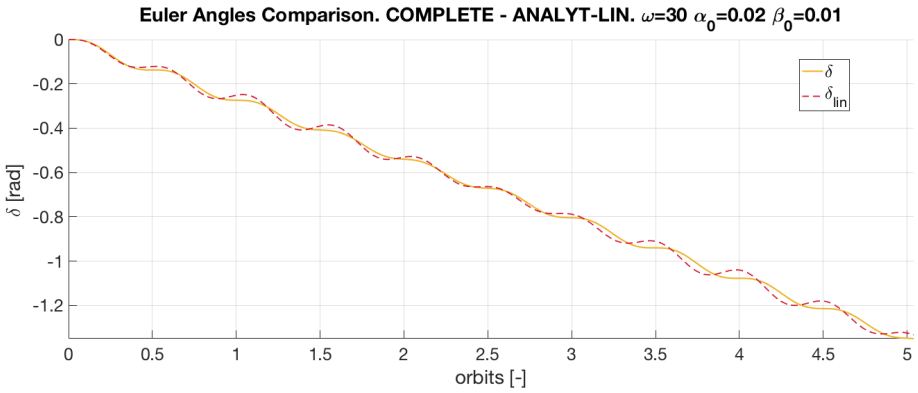

Fig. 4.13. δ perturbation for $\tilde{\omega}$=30 and non zero IC

Finally, the following figures 4.14 and 4.15 show the same check performed in the previous section, squared quaternion component sum and kinetic energy evolution in time.

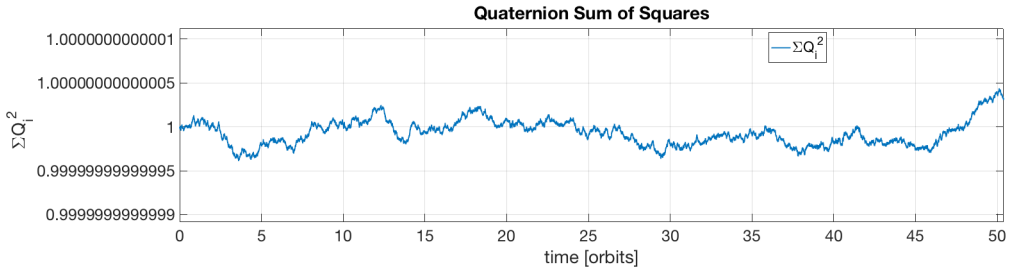

Fig. 4.14. quaternion squared sum check of the nonlinear system

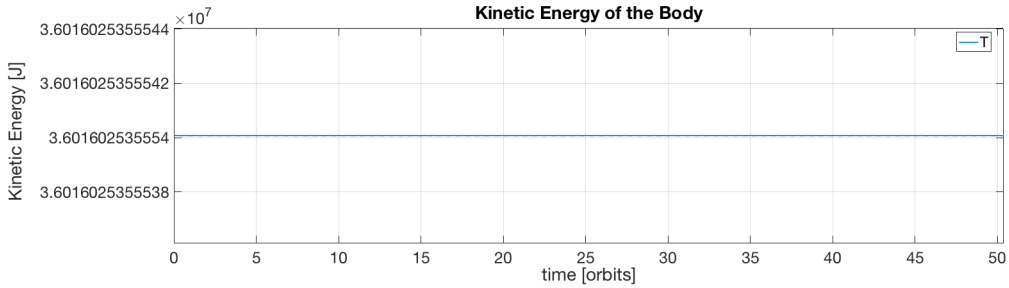

Fig. 4.15. kinetic energy of the nonlinear system

As an important remark, it is not shown in any figure, but simulations were performed with both IC and $\tilde{\omega}$ set to zero and as it was expected, all the results obtained were zero. This makes sense physically, once gyroscopic effects are zero, in this particular initial

position each of the symmetric satellite differentials of mass is at the same distance to the Earth and hence, the gravitational gradient acts equally over them, balancing all the differential torques.

4.3. Camera model

In this section, the results obtained from the equations of the cameras of section 3.6 will be analyzed and camera angles readings extracted from different simulated scenarios will be interpreted and compared to the theoretically unknown values of Euler angles to try to retrieve by inspection the value of the initial condition of the roll angle α_0.

4.3.1. Camera angles

As it was expected the figures 4.16, 4.17 and 4.18 show the expected results of the angles obtained by the cameras of the horizon sensors.

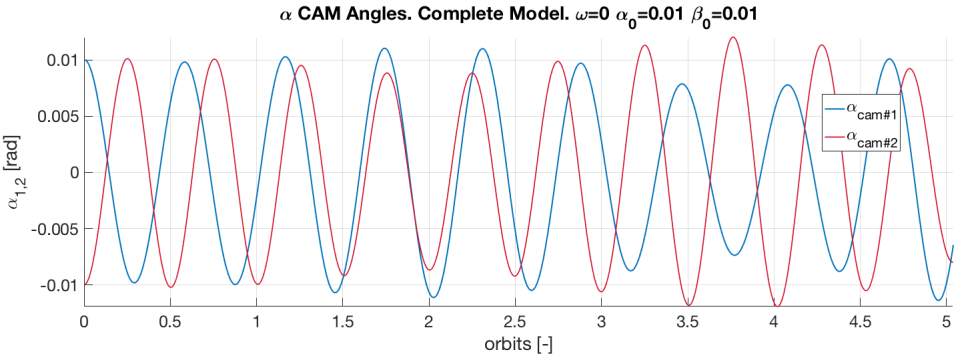

Fig. 4.16. α_1 and α_2 angles for $\tilde{\omega}$=0

Figure 4.16 shows in a more clear way the correspondence stated in equations 3.74 and 3.75 based on the initial conditions of the simulation. Having a zero spin value, the oscillations match accurately in both amplitude and period with Euler Angles.

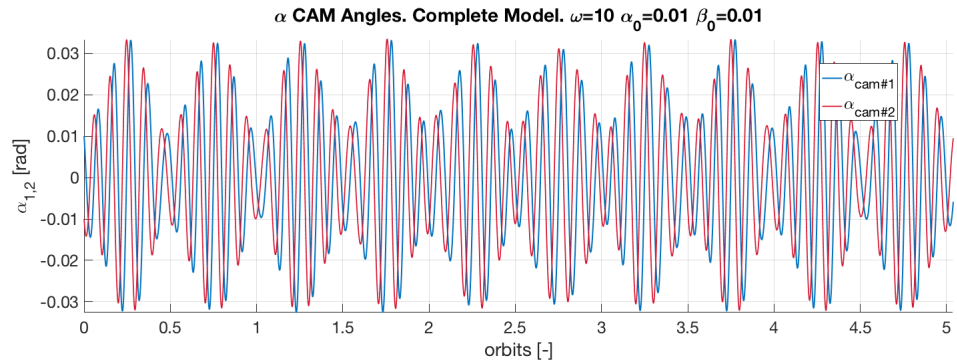

Fig. 4.17. α_1 and α_2 angles for $\tilde{\omega}$=10

Figures 4.17 and 4.18 picture the effect of the increase in adimensional spin $\tilde{\omega}$ to 10 and 30, which result in a high increase in frequency of the oscillations.

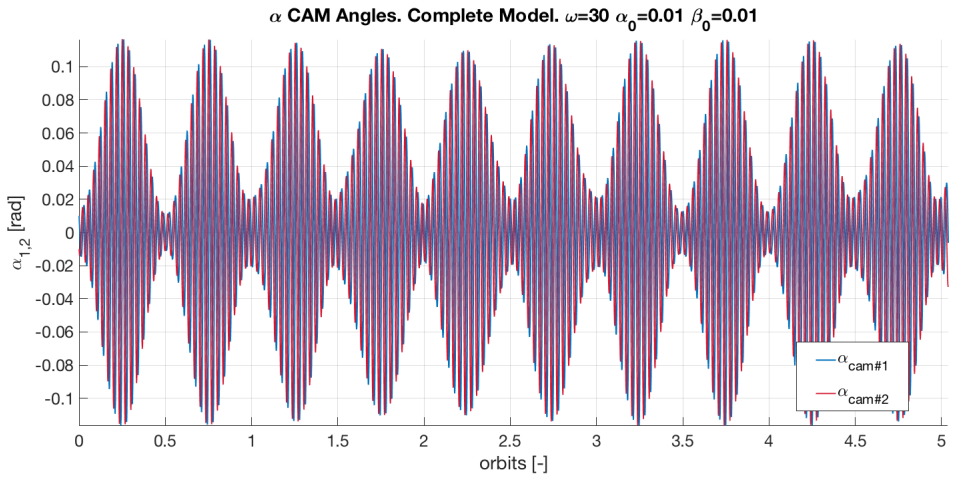

Fig. 4.18. α_1 and α_2 angles for $\tilde{\omega}$=30

4.3.2. Cam angles vs Euler angles example

A couple of examples comparing the camera angles and the attitude of the corresponding Euler axes of rotation (cam-1 vs pitch and cam-2 vs roll) are shown below.

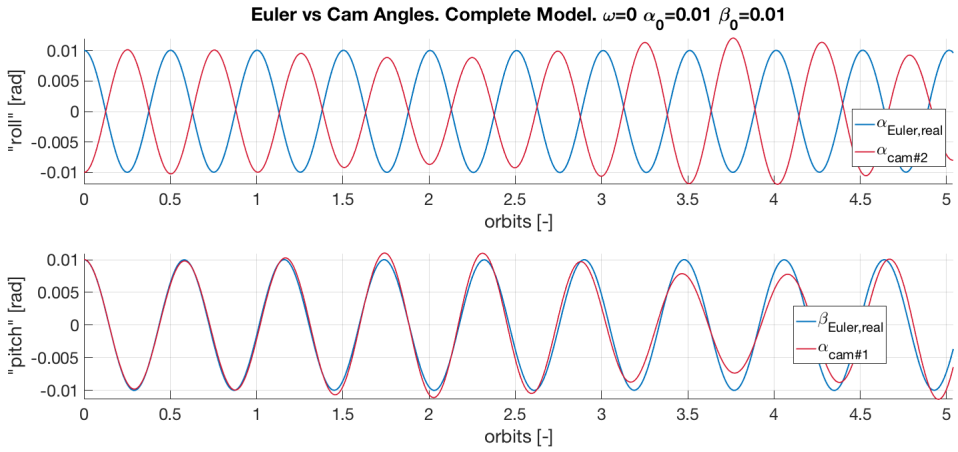

Fig. 4.19. α_1 and α_2 vs EA α and β for $\tilde{\omega}$=0

It is interesting to see that knowing the positioning of the cameras, for a zero spin, the Euler angles α and β are almost completely determined by inspection. Of course, without taking into account errors coming from the cameras or any other source of error.

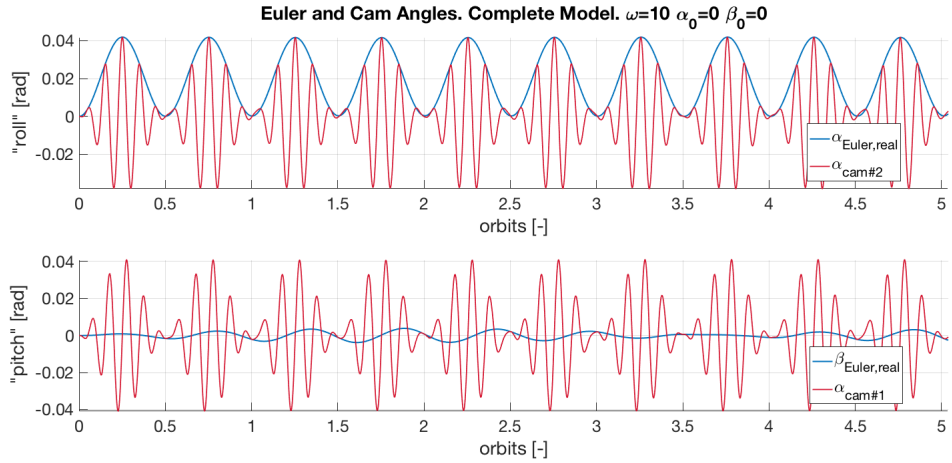

Fig. 4.20. α_1 and α_2 vs EA α and β for $\tilde{\omega}$=10

In figure 4.20, only the angle α could be retrieved from inspection, knowing in advance the value of the adimensional spin, $\tilde{\omega}$.

4.3.3. Initial guess for roll angle IC

The following set of figures have been extracted to illustrate the idea of obtaining the α_0 by inspection to help the further implementation of the attitude determination algorithm. Several possible situations have been simulated to try to be more precise in the initial guess of α_0.

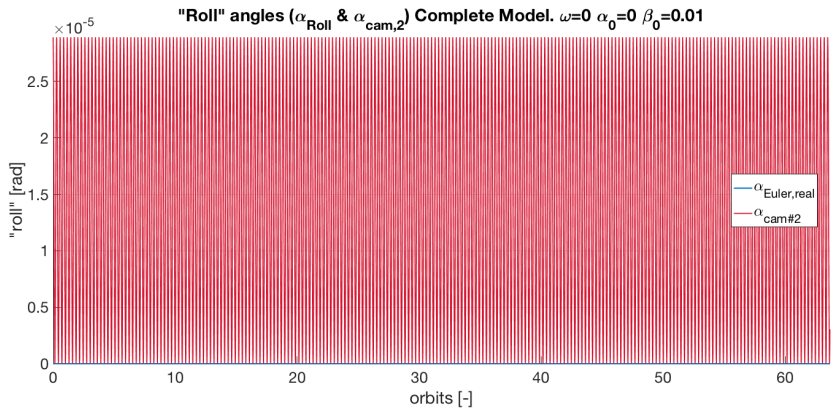

Fig. 4.21. α_2 vs α Euler for $\tilde{\omega}$=0 zero α_0, non zero β_0

Figures 4.21 to 4.25 show both the α angle (Euler) and the angle coming from the second camera for spin velocity zero.

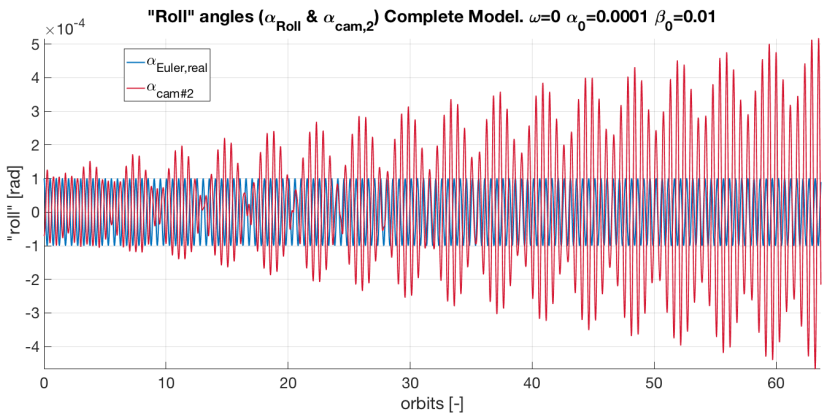

Fig. 4.22. α_2 vs α Euler for $\tilde{\omega}$=0 close to zero α_0, non zero β_0

As it can be seen, varying the value of the initial condition of α, the maximum values of oscillation of the camera angle pictured are also varying. By inspection, observing the camera angles amplitude in each of the scenarios and taking the maximum or even the medium value of its oscillations, the initial guess for α_0 is near to be the exact one.

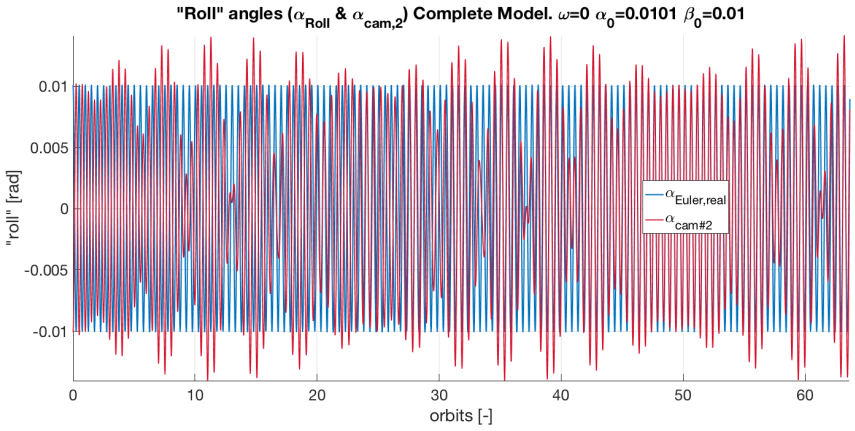

Fig. 4.23. α_2 vs α Euler for $\tilde{\omega}$=0 non zero α_0, non zero β_0

As α_0 increases, the amplitude of the oscillations becomes larger, and it is seen that when β_0 is not zero, it results in perturbations of the smoothness of the camera angle.

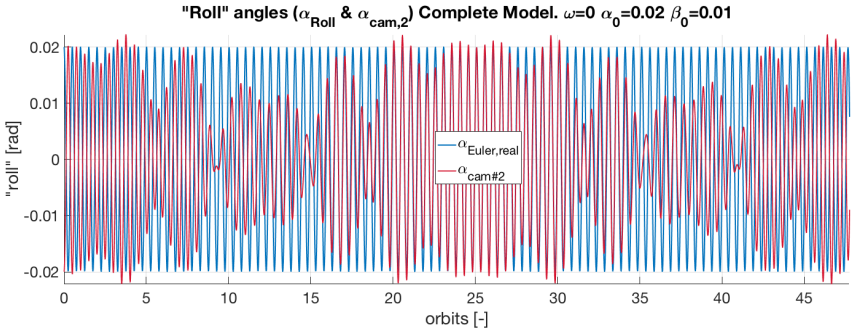

Fig. 4.24. α_2 vs α Euler for $\tilde{\omega}$=0 non zero α_0, non zero β_0

The last figure 4.25 of the $\tilde{\omega} = 0$ scenario shows the results of a zero initial pitch angle. The camera angle oscillation's amplitude rate of change becomes smooth, almost parabolic. And the determination of the initial value α_0 through the global maximum is perfect.

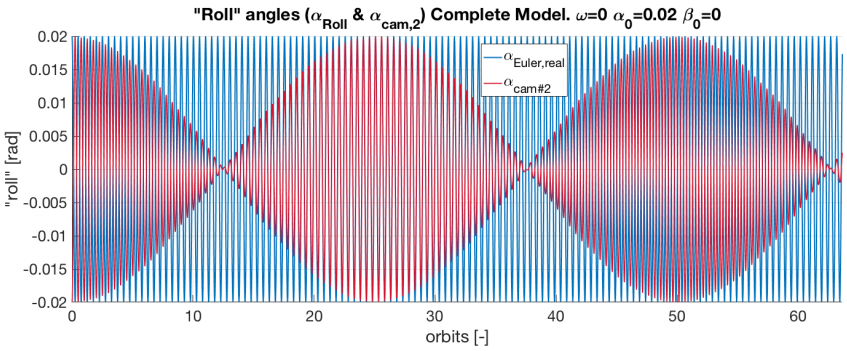

Fig. 4.25. α_2 vs α Euler for $\tilde{\omega}$=0 non zero α_0, zero β_0

Now, figures 4.26 and 4.27 are shown below,

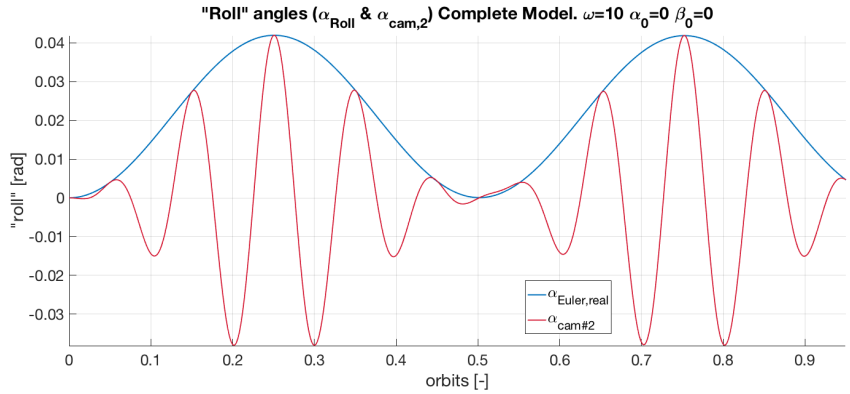

Fig. 4.26. α_2 vs α Euler for $\tilde{\omega}$=10 zero α_0, zero β_0

when the spin is higher, and consequently the *roll-bias* is significant, the determination of α_0 and the whole roll angle is possible.

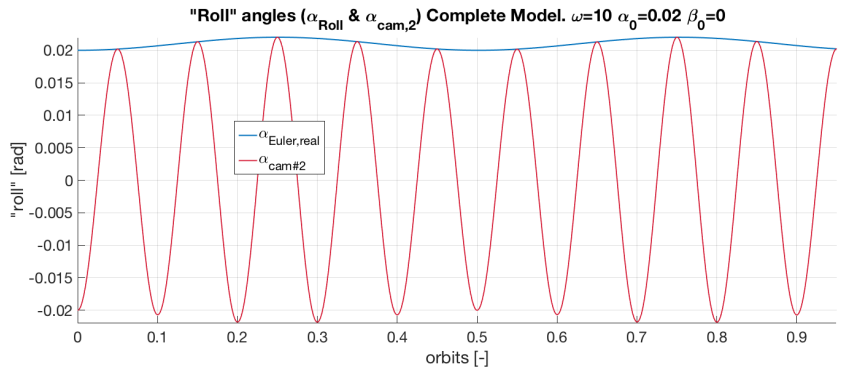

Fig. 4.27. α_2 vs α Euler for $\tilde{\omega}$=10 non zero α_0, zero β_0

4.4. Optimization results

The basic operation of the algorithm was explained in section 3.7. In this section, the results obtained for the constants have been input into the analytical equations and compared to the the input of the real initial conditions. For all the cases the algorithm was run for a sample of little over 5 orbits.

The first scenario, as expected, the lack of gyroscopic effects brings a perfect match between the solutions

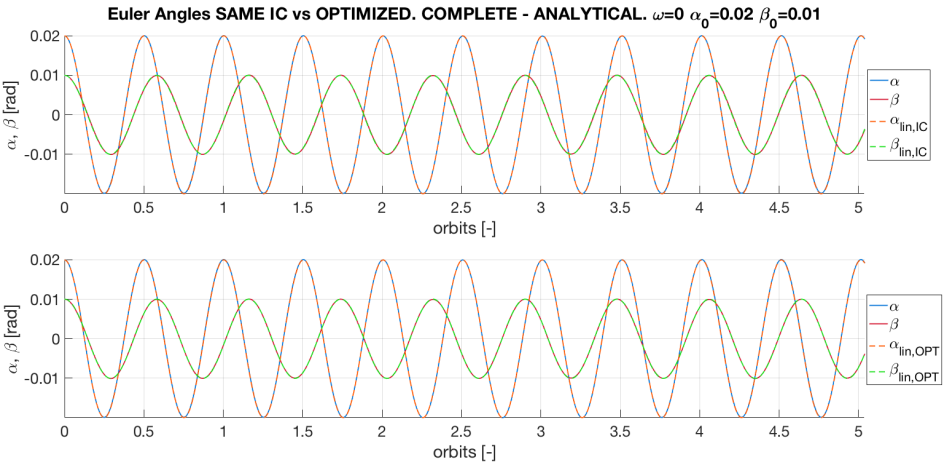

Fig. 4.28. α and β angles for $\tilde{\omega}$=0 and non zero IC

all the Euler angles are matched perfectly

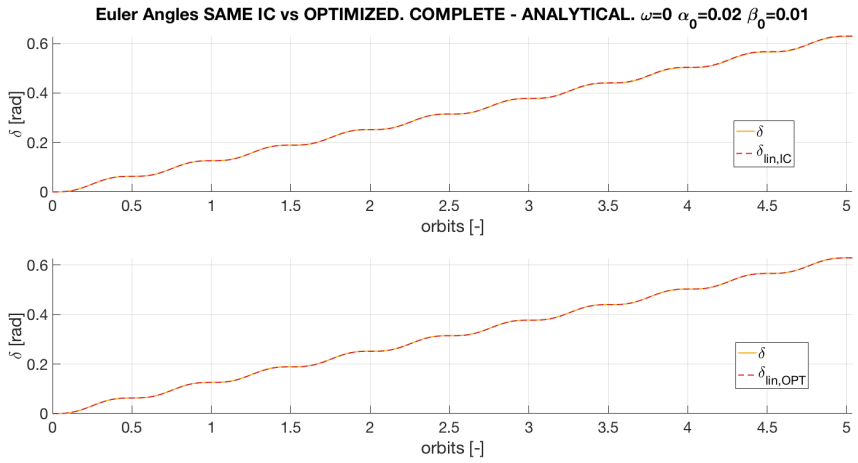

Fig. 4.29. δ perturbation for $\tilde{\omega}$=0 and non zero IC

As it was shown in section 4.2, the effect of the a considerably high spin velocity starts to affect the linear theory results,

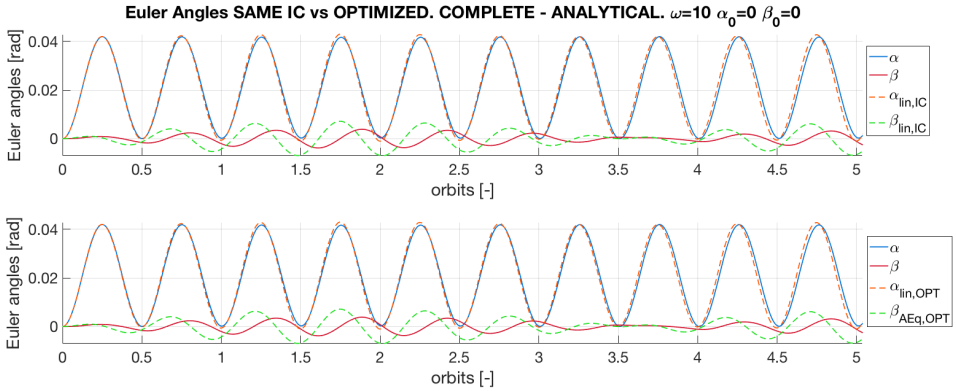

Fig. 4.30. α and β angles for $\tilde{\omega}$=10 and zero IC

as it can be seen from figures 4.30 and 4.31, the algorithm retrieved accurate values for α and δ. Due to linear effects, β_{opt} replicates almost identically what the same initial conditions provide. The algorithm has provide perfect results so far.

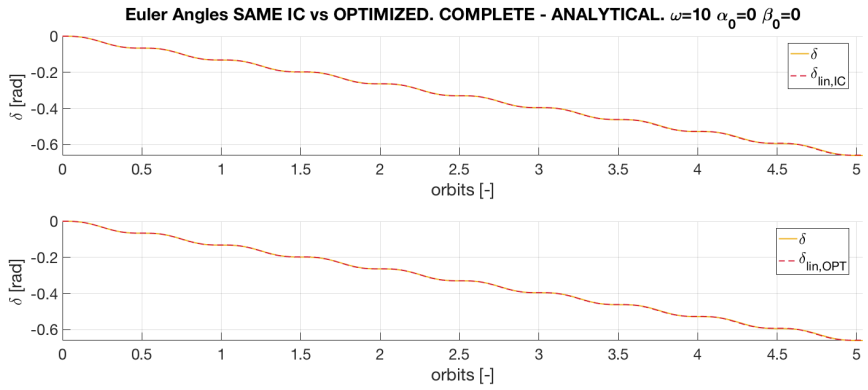

Fig. 4.31. δ perturbation for $\tilde{\omega}$=10 and zero IC

For the same spin velocity, when applying non zero initial conditions, the algorithm works a little bit differently.

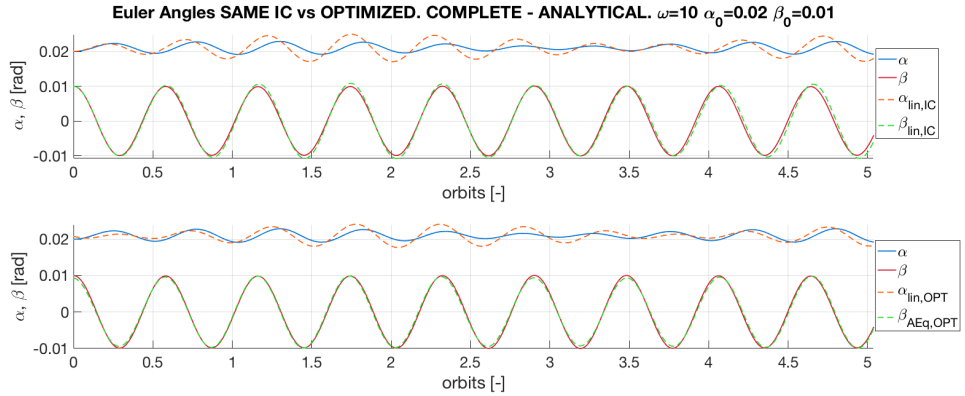

Fig. 4.32. α and β angles for $\tilde{\omega}$=10 and non zero IC

Firstly, the accuracy in determining β is a little bit higher than the same IC case, although

linear theory produced subtle errors on it. The interesting case comes from α and δ angles. The algorithm improved the prediction of α, reducing the difference in amplitude of the same initial conditions case.

However, δ_{opt} has lost the correct slope that the true initial conditions provide. For small times this is not a problem, but the accumulated error should be taken into account in the future and a correction factor over the slope of δ_{opt} could be implemented. This clear deviation is shown in 4.33

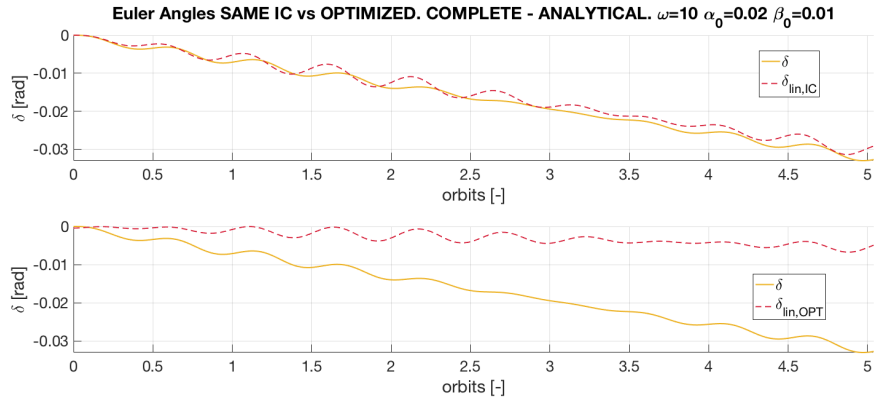

Fig. 4.33. δ perturbation for $\tilde{\omega}$=10 and non zero IC

The last scenario, as it is known, provides larger errors due to larger nonlinear effects.

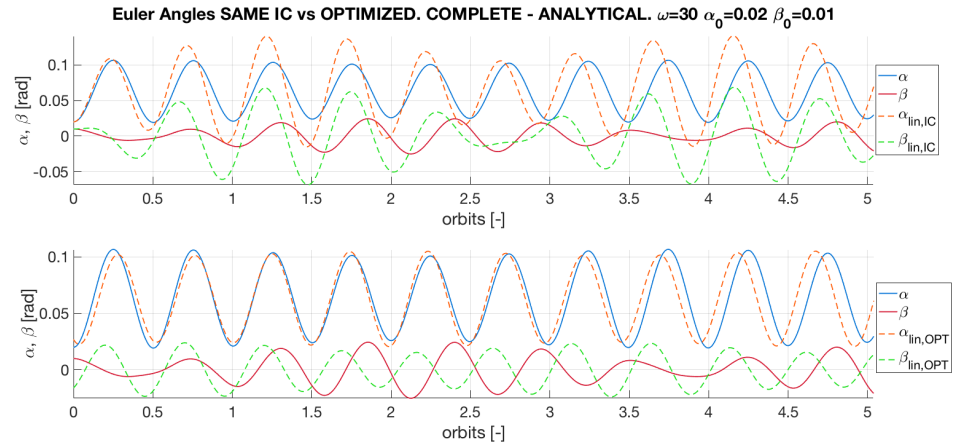

Fig. 4.34. α and β angles for $\tilde{\omega}$=30 and non zero IC

In this case, the algorithm worked much better than the original IC. By changing the value of the initial conditions and maintaining the value of $\tilde{\omega}$, the algorithm has been able to predict the angles more accurately. Amplitudes of α and β are almost perfect, finding less accuracy in the phase of β. Referring to the prediction of δ perturbation, a little offset in the value of the slope is found with respect to the solution of the true IC. Again, this is minor issue as delta is just the perturbation of the yaw angle γ, defined in section 3.5.2

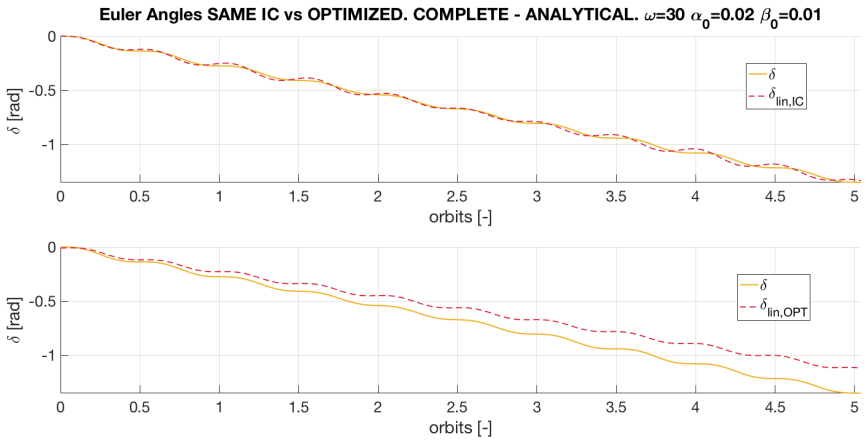

Fig. 4.35. δ perturbation for $\tilde{\omega}$=30 and non zero IC

4.5. Minimum Mean Square Error variation. Optimization effectiveness range

In this section, the resultant minimum values retrieved from the inbuilt MATLAB function *fminsearch* operation on the MSE function described in 3.7 will be analyzed. The calculations have been made on a range of values of time span and step size.

4.5.1. Time span variation

The selected range of time span values is 500 to 33000 seconds, with 30 measurements in total.

The first scenario of *omẽga* = 0 shows very accurate results (or very small dispersion error) as it was observed in the previous section.

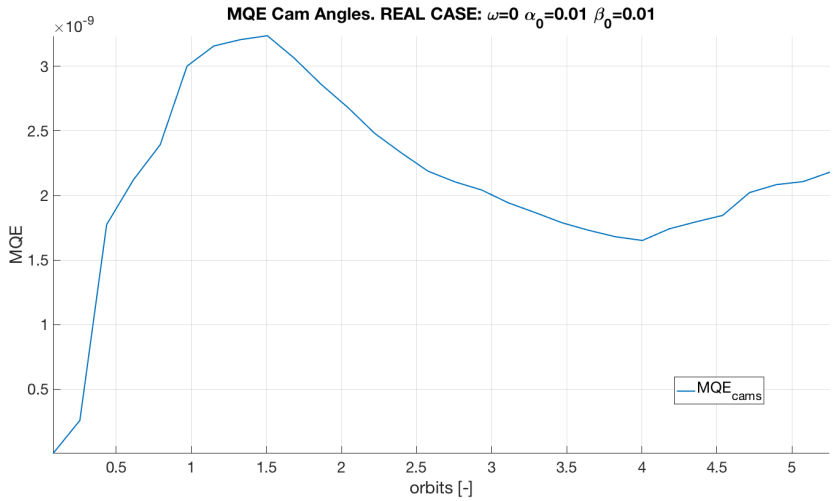

Fig. 4.36. Cam angles MQE for $\tilde{\omega}$=0. Time span variation

by looking at figure **??** the minimum MSE stabilizes at 1.5 orbits, this should be taken into

account in order to select the sample within the algorithm. The maximum error caused was found to be on δ. This could make sense as it the most difficult angle to predict.

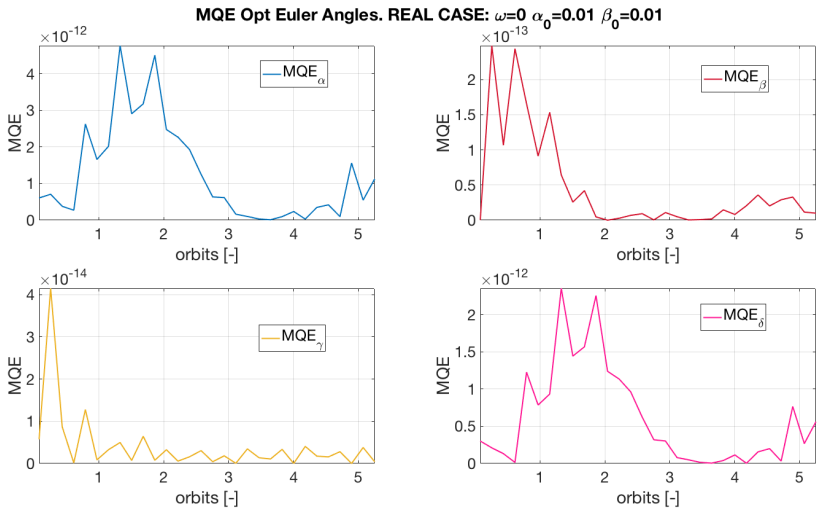

Fig. 4.37. Euler angles MQE for $\tilde{\omega}$=0. Time span variation

Increasing the spin, increases the minimum MSE. The algorithm is subjected to the effects of linear theory and hence, larger gyroscopic effects will always result in larger minimum MSE values.

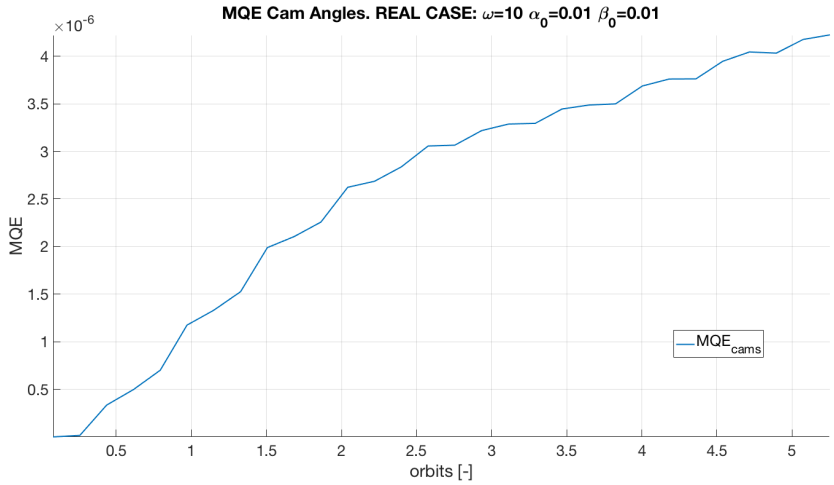

Fig. 4.38. Cam angles MQE for $\tilde{\omega}$=10 non zero IC. Time span variation

The minimum MSE of the cameras is changed by one order of magnitude (reduced), although it has not been stabilized. The corresponding change in MSE for the Euler angles is of 2 orders of magnitude for β and δ and one order for α and γ.

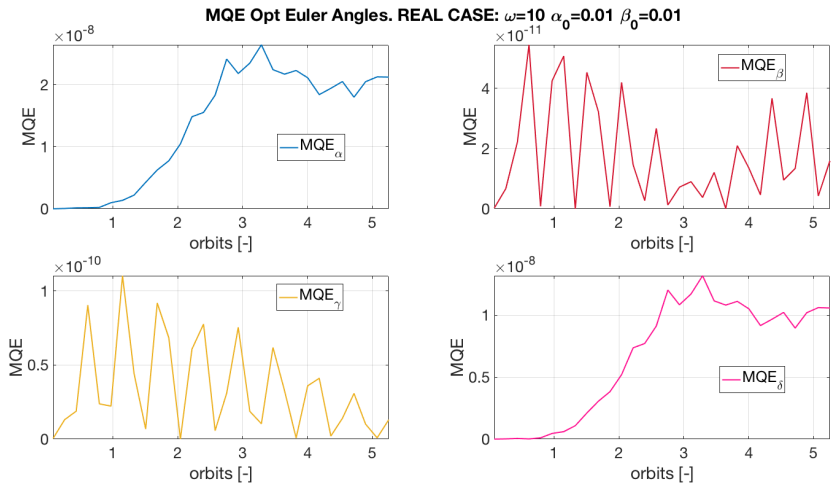

Fig. 4.39. Euler angles MQE for $\tilde{\omega}$=10 non zero IC. Time span variation

The last scenario, turning the initial conditions to zero, does not affect the order of magnitude of the cams MSE and consequently, neither does in the Euler angles MSE

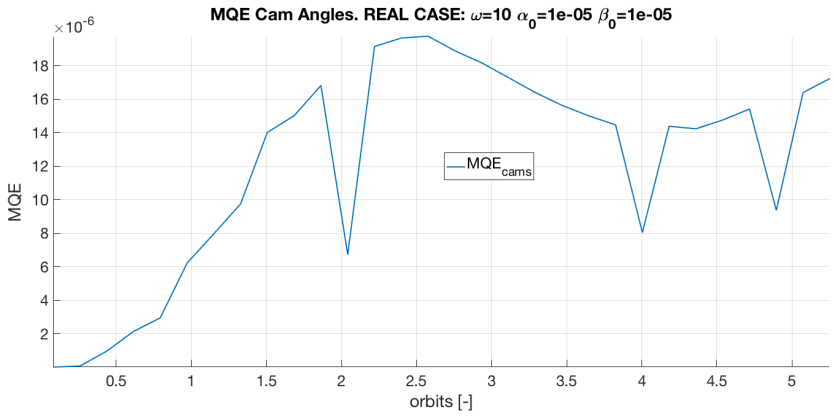

Fig. 4.40. Cam angles MQE for $\tilde{\omega}$=10 close to zero IC. Time span variation

similar patterns of minimum MSE in function of time are found for α and δ in all the scenarios

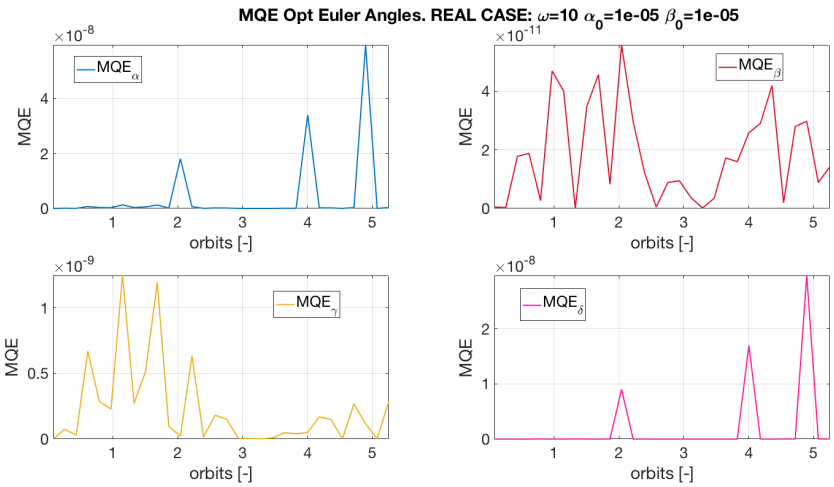

Fig. 4.41. Euler angles MQE for $\tilde{\omega}$=10 close to zero IC. Time span variation

4.5.2. Step size variation

The selected range of values for the step size is 0.1 to 0.5 seconds with a sample of 17 and during an integration time span of 12700 seconds or 2 orbits approximately.

Figures 4.42 to 4.47 will be commented in pack as they do not provide much information separately.

The variation of the minimum cams MSE in function of the step size ranges between the order of 10^{-6} and 10^{-5}, so really small differences will be perceived in the following figures. Hence, for the sake of computational issues, large step size can be selected and consequently, a smaller sample. This will result in less computational expenses maintaining the quality of the algorithm.

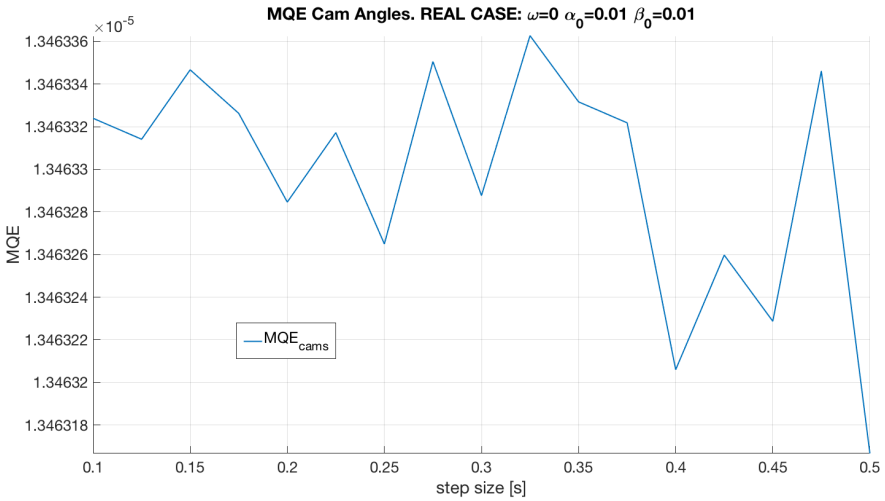

Fig. 4.42. Cam angles MQE for $\tilde{\omega}$=0. Step size variation

The largest error is found on beta in this case

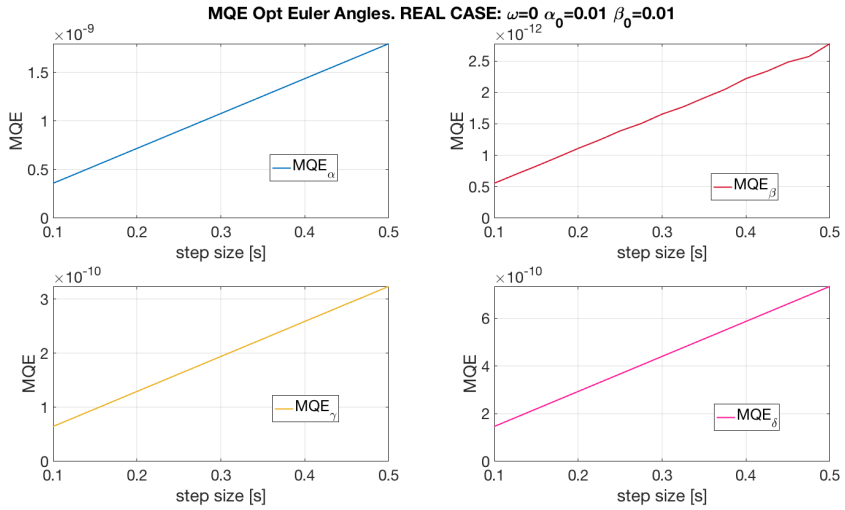

Fig. 4.43. Euler angles MQE for $\tilde{\omega}$=0. Step size variation

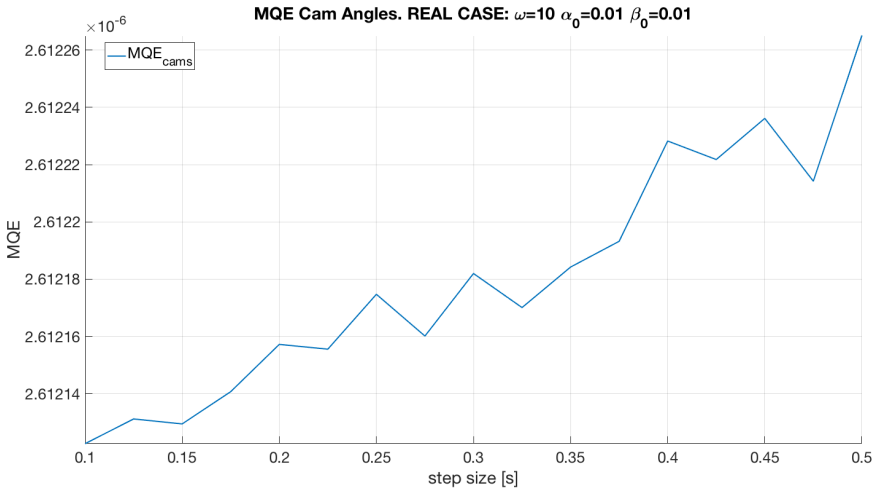

Fig. 4.44. Cam angles MQE for $\tilde{\omega}$=10 non zero IC. Step size variation

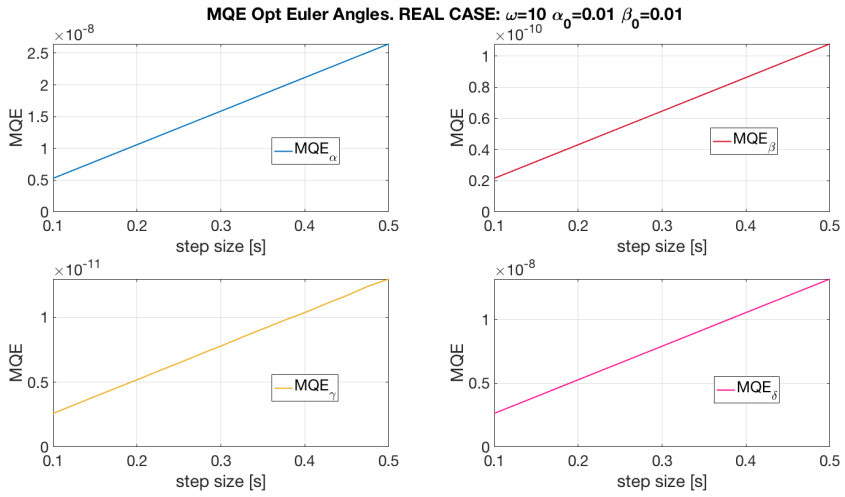

Fig. 4.45. Euler angles MQE for $\tilde{\omega}$=10 non zero IC. Step size variation

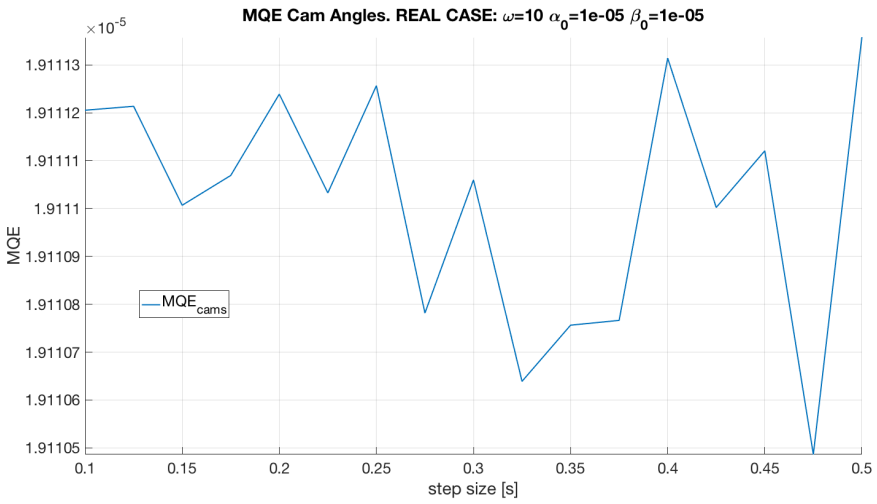

Fig. 4.46. Cam angles MQE for $\tilde{\omega}$=10 close to zero IC. Step size variation

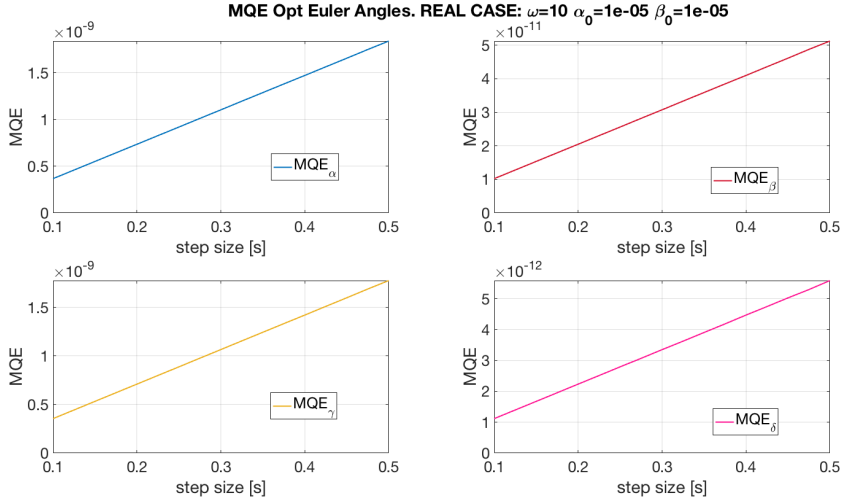

Fig. 4.47. Euler angles MQE for $\tilde{\omega}$=10 close to zero IC. Step size variation

5. CONCLUSIONS

In this work, the development of an algorithm capable of determining the attitude of a slender body satellite by only using two horizon sensors was implemented.

The results obtained in chapter 4 were very concrete about the high accuracy of the algorithm in determining the satellite's attitude within the proposed model. Implementing a two horizon sensor configuration, a system to obtain the spin angular velocity (probably a gyroscope) and the proposed algorithm into an onboard computer is shown to be enough to predict values of the attitude of the satellite with a max attitude MSE of the order of 10^{-8} for a spin angular velocity of $\tilde{\omega} = 10$

However, the proposed problem is bounded by the assumptions and simplifications explained in chapters 2 and 3, which may differ considerably from a real low orbit scenario. Applying a more realistic orbit and taking into account other sources of disturbance torques, such as solar radiation, would reduce the effectiveness of the algorithm. Besides, several other aspects should be taken into account in order to select an Attitude Determination and Control System [20], like the system budget, payload and design constraints (possibly cancelling the slender body hypothesis).

6. FUTURE WORK

As mentioned at the end of chapter 5, the future work should be focused on the actualization of the algorithm based on a new, more realistic model.

This model could include, for example, the implementation of new disturbance torques apart from the gravity gradient such as solar radiation, aerodynamic drag (altitude dependent), magnetic torques, mass expulsion or internally generated torques [20]. All of them will affect in a different way adding new nonlinearities to the problem and new sources of error.

Moreover, next step could also be taking into account the error of the horizon sensor camera angle determination or the error of the determination of the spin angular velocity.

Finally, the implementation of a complex Precision Algorithm, which could be able to change the slenderness of the satellite (unfolding certain structures, for example) in function of the desired application.

BIBLIOGRAPHY

[1] M. Wall. (2019). Spacex launches historic crew dragon test flight, [Online]. Available: https://www.space.com/spacex-launches-crew-dragon-test-flight.html.

[2] U. N. O. for Outer Space Affairs. (2019). Space object register, [Online]. Available: http://www.unoosa.org/oosa/en/spaceobjectregister/index.html.

[3] T. Wekerle, J. B. Pessoa Filho, L. E. V. L. d. Costa, and L. G. Trabasso, "Status and trends of smallsats and their launch vehicles—an up-to-date review", *Journal of Aerospace Technology and Management*, vol. 9, no. 3, pp. 269–286, 2017.

[4] Wikipedia. (2019). Cubesat, [Online]. Available: https://en.wikipedia.org/wiki/CubeSat.

[5] A. Klesh and J. Krajewski, "Marco: Cubesats to mars in 2016", 2015.

[6] T. Nguyen, K. Cahoy, and A. Marinan, "Attitude determination for small satellites with infrared earth horizon sensors", *Journal of Spacecraft and Rockets*, vol. 55, no. 6, pp. 1466–1475, 2018.

[7] S. I. Association, "State of the satellite industry, 2019", *Advances in the Astronautical Sciences*, 2019.

[8] J. Amos. (2019). Oneweb launches mega-constellation pathfinder satellites, [Online]. Available: https://www.bbc.com/news/science-environment-47374246.

[9] J. Foust. (2018). Tiangong-1 reenters over south pacific, [Online]. Available: https://spacenews.com/tiangong-1-reenters-over-south-pacific/.

[10] D. J. Kessler, N. L. Johnson, J. Liou, and M. Matney, "The kessler syndrome: Implications to future space operations", *Advances in the Astronautical Sciences*, vol. 137, no. 8, p. 2010, 2010.

[11] NASA. (2017). Cubesat101 basic concepts and processes for first-time cubesat developers, [Online]. Available: https://www.nasa.gov/sites/default/files/atoms/files/nasa_csli_cubesat_101_508.pdf.

[12] E. O. Portal. (2019). Micromas-1, [Online]. Available: https://directory.eoportal.org/web/eoportal/satellite-missions/content/-/article/micromas-1.

[13] R. A. Hutchin, "Earth horizon sensor", US 2011/0004405 A1, 2011.

[14] N. Air and S. Museum. (2019). Horizon sensor, [Online]. Available: https://airandspace.si.edu/collection-objects/horizon-sensor.

[15] J. Rodríguez, “Aspectos matemáticos de la determinación de actitud mediante sensores de horizonte”, *E.T.S.I. Aeronáuticos, Universidad Politécnica de Madrid*, 1996.

[16] J. Rodríguez and J. Santiago, “Dinámica del giróscopo esbelto bajo la acción de un gradiente de gravedad”, *E.T.S.I. Aeronáuticos, Universidad Politécnica de Madrid*, 1998.

[17] K. Großekatthöfer and Z. Yoon, “Introduction into quaternions for spacecraft attitude representation”, *TU Berlin*, vol. 16, 2012.

[18] Y.-B. Jia, “Quaternions and rotations”, *Com S*, vol. 477, no. 577, 2008.

[19] J. C. Lagarias, J. A. Reeds, M. H. Wright, and P. E. Wright, “Convergence properties of the nelder–mead simplex method in low dimensions”, *SIAM Journal on optimization*, vol. 9, no. 1, pp. 112–147, 1998.

[20] J. R. Wertz, *Spacecraft attitude determination and control*. Springer Science & Business Media, 2012, vol. 73.

[21] F. L. Markley and J. L. Crassidis, *Fundamentals of spacecraft attitude determination and control*. Springer, 2014, vol. 33.

[22] S. Sarabandi and F. Thomas, “Accurate computation of quaternions from rotation matrices”, pp. 39–46, 2018.

[23] B. Etkin and L. D. Reid, *Dynamics of flight*. Wiley New York, 1959, vol. 2.

[24] E. Garcıa López, “Determinación de la actitud de un satélite utilizando un único sensor de horizonte”, Master’s thesis, 2010.

[25] A. García López, “Earth-moon low energy trajectory generation”, Master’s thesis, 2018.

[26] V. Gorev, A. Pelemeshko, A. Zadorozhny, and A. Sidorchuk, “Thermal deformation of 3u cubesat in low earth orbit”, in *MATEC Web of Conferences*, EDP Sciences, vol. 158, 2018, p. 01 013.

[27] A. Froehlich, *Legal Aspects Around Satellite Constellations*. Springer, 2019.